Volume, Heat and Freshwater Transports of the Global Ocean Circulation 1992 –1997, Estimated from a General Circulation Model Constrained by WOCE Data

D. Stammer[1], C. Wunsch[2], R. Giering[3] C. Eckert[2], P. Heimbach[2],
J. Marotzke[4], A. Adcroft[2], C.N. Hill[2], and J. Marshall[2]

August 23, 2001

Submitted to J. Geoph. Research

[1]Corresponding Author: Detlef Stammer, Scripps Institution of Oceanography
[2]Massachusetts Institute of Technology
[3]FastOpt, GBR, Hamburg
[4]Southampton Oceanographic Center

Abstract

An analysis of ocean volume, heat and freshwater transports from a fully constrained general circulation model is described. Output from a data synthesis, or state estimation, method is used by which the model was forced to a large-scale, time varying global ocean data set over six years. Time-mean fluxes estimated from this fully time-dependent circulation have converged with independent time-independent estimates from box inversions over most parts of the world ocean but especially in the southern hemisphere. However, heat transport estimates differ substantially in the North Atlantic where our estimates result in only 1/2 previous heat transports.

The estimated mean circulation around Australia involves a net volume flux of 14 Sv through the Indonesian Throughflow and the Mozambique Channel. In addition we show that this flow regime exist on all time scales above one month rendering the variability in the South Pacific strongly coupled to the Indian Ocean. Moreover, the dynamically consistent variations in the model show temporal variability of oceanic heat fluxes, heat storage and atmospheric exchanges that are complex and with a strong dependence upon location, depth, and time-scale. Results presented demonstrate the great potential of an ocean /state estimation system to provide a dynamical description of the time-dependent observed heat transport and heat content changes and their relation to air-sea interactions.

1 Introduction

One of the purposes of the World Ocean Circulation Experiment (WOCE) has been to achieve a full synthesis of the global observations to determine the general circulation and its transport variability over an extended period. This goal can be reached by bringing a full ocean circulation model into consistency with the diverse ocean observations and using the combination to study the circulation, its energetics, driving forces, property fluxes, dynamical balances, and the nature and structure of its variability, among many other problems.

In a previous paper (*Stammer et al.,* 2001a, hereafter Paper 1), we described the overall results from an initial attempt at a combination of a general circulation model (GCM) with much of the existing global data from a six year interval 1992 – 1997, in a procedure called "state estimation" or "data assimilation". In contrast to a number of other such attempts (e.g., Carton et al., 2000a,b), a deliberate decision was made to use a very general method—one that could become rigorous as computer power grows and as knowledge of the underlying statistics improves—at the expense of a greater computational load. Imposed data included both mean and time-varying altimetry, hydrographic climatologies, as well as the estimated air-sea fluxes of momentum, fresh water and heat from twice-daily atmospheric estimates. Paper 1 provides details of the method (Lagrange multipliers, or adjoint), the optimization and some general tests of the adequacy of the model-data combination. In particular, it shows that the constrained model displays considerable skill in reproducing both the observations, and much of the withheld data. Remaining discrepancies can lie with either the model, the data, or both, and require further information to resolve. Despite various lingering issues, an overall conclusion was that the constrained model displays considerable skill in reproducing the observations, and in particular with qualitative and quantitative features of the withheld data. We therefore begin here to exploit the results for scientific purposes.

Our focus is on the determination of the ocean fluxes of volume, heat and freshwater and their divergences that appear to be most important to understanding the climate

system. Because the first year of the optimization shows some residual signs of adjustment problems, we base the following analysis on the last five years of the optimized estimate. A more detailed analysis of associated surface heat, freshwater, and momentum fluxes and their uncertainties will be described elsewhere (*Stammer et al.*, 2001b). Because of: (1) the nature of the T/P data set which best constrains the time variability on time scales out to about five years, and (2) concerns about adequate model resolution, we believe that the temporal variability of properties in our results is considerably more accurate than is the time average or absolute values. Thus, while we describe the time average results, most of our emphasis will be on discussing the fluctuating components.

In the absence so far, because of the computational load, of a formal full error analysis of the estimated ocean state, comparisons with independent estimates of various quantities are used to build up an empirical depiction of the overall accuracy of the results. Obtaining realistic property fluxes, such as those for temperature, puts stringent demands on a model: the transports are second-order quantities, involving products of velocities and property distributions; models that produce sensible-appearing flow and temperature fields may well fail to estimate accurately integrated products of these fields.

The results reported are believed to be the first obtained from a general circulation model whose quantitative consistency with complete global data sets has been enforced in a dynamically consistent way. More applications exist than the one described here; for example, *Ponte et al.* (2001), used the same results to study the Earth's angular momentum balance, and efforts to calculate the corresponding biogeochemical fluxes are underway.

An indication of the skill of the present analysis can be found in Fig. 1 which depicts Fig. 1
the depth of the 20°C isotherm as measured from six years of TOGA-TAO (Tropical Ocean Global Atmosphere-Tropical-Atmosphere-Ocean) measurements (*McPhaden et al.*, 1998) on the equator between (140°-150°E) and at 265°E. Despite gaps, one sees the clear signal of the 1992/93, 1994/95 and the 1997 Niños events. Also shown are the respective results from the unconstrained and constrained models. While the unconstrained model produces

a fairly constant isotherm depth in the west, and loses the warm water altogether in the east, the constrained result shows much better agreement with the observations. The model skill illustrated in the figure is noteworthy given the low resolution of the model and the fact that none of the TAO or expendable bathythermograph (XBT) data were used to constrain the model.

The figure also shows the east-west gradient of the 20°C isotherm as simulated by the unconstrained and constrained models. Three recent ENSO events show up as substantially reduced east-west slopes in the isotherm, followed by a rapid reversal of this tendency during the subsequent build-up phase in the constrained system. Although some seasonal-to-interannual variability is superimposed, the unconstrained model does not simulate the decrease in thermocline slope during the last El Niño.

While the TAO measurements have obvious data gaps, the model is continuous. It tracks the data where they exist and allows one to infer changes and their dynamics even where no data exist. A goal of data assimilation is therefore to use the estimated model state everywhere (in space and time) to infer variables that are not directly observed, such as heat content over large regions or heat transports into those regions.

The heat content of volume V is,

$$Q = \rho c_p \int\int\int_V \theta dz dx dy, \tag{1}$$

where c_p is the specific heat capacity, and ρ the water density. One fundamental question is whether the model simulates, e.g., large scale changes in heat content that are consistent with independently observed interannual to decadal scale climate variations? To answer this question, we computed from the unconstrained and constrained models large-scale heat content variations over the top 800 m depth and compared those estimates with similar ones obtained from XBT data. During the computation, the model fields were first interpolated onto the XBT positions in space and time, thus providing the identical sampling characteristics in all estimates.

Characteristic results are shown in Fig. 2 for two rectangular regions spanning 20° of latitude and longitude, which are centered at 190°E, 30°N; and at 150°E, 10°S. One Fig. 2

sees that the unconstrained model shows a reasonable amount of interannual variability reflecting most of the observed changes, and which are driven by the NCEP surface forcing fields. Remaining differences between the model and the XBT observations are largely removed in the constrained model. The differences so removed can be interpreted (but not uniquely so) as a measure of errors in the atmospheric forcing fields. Because the primary source of information for the time-variations is the altimeter data the large information content of these observations is apparent.

Section 2 describes the estimated volume transports. Mean transports of heat and freshwater and their relations to surface fluxes will be described in Section 3, with a discussion of the dynamics of temporal variability of heat fluxes and their variability in Section 4. A formal computation of regional heat content changes and their relationship to lateral and vertical transport processes and surface forcing is in Section 5.

2 Volume Fluxes

The underlying MIT GCM uses the Boussinesq approximation, and volume transport is the appropriate surrogate for mass movement (*Marshall et al.*, 1997). The mean horizontal transport of volume across an ocean basin of width L, and depth $h(x)$, is defined, conventionally, as

$$H_V = \int_0^L \int_{-h(x)}^0 v\,(x,z)\,dzdx, \tag{2}$$

where v is the velocity component normal to the section as shown in Fig. 3a. In the figure we show the mean and standard deviation of H_V across several sections which coincide with nominal positions of WOCE one-time hydrographic sections. Because the northern model boundary is closed, there is no exchange across the Arctic, and mean meridional volume fluxes in the Northern Hemisphere are zero. The few estimates of the flux into the Arctic (e.g., *Roach et al.*, 1995)) suggest that less than 1 Sv is involved; it will be included in future computations. Fig.3

While time-mean volume fluxes into enclosed basins are zero, their variability is not,

indicating high-frequency storage effects over the larger basins such as the North Pacific or North Atlantic. Standard deviations of volume fluxes at about 25°N are slightly larger than 1 Sv in both basins and are associated with a 0.5 cm high-frequency fluctuation of sea level on basin scale. Those flux variations occurring at very high frequencies are dominated by the rapid wind-induced Ekman transport and an associated barotropic return flow (see also *Fukumori et al.*, 1998; *Stammer et al.*, 2000; *Tierney et al.*, 2000; *Jayne and Marotzke,* 2001). This and other variability is strongly constrained by the relatively dense altimetric data sets.

In contrast to enclosed basins that do not show any long-term gain or loss of volume, closed flow loops do show net fluxes. The most conspicuous one is the mean anticyclonic circulation around Australia, where about a total of 14 Sv flow northward in the South Pacific, through the Indonesian Throughflow, and returning southward through the Mozambique Channel. In the Indian Ocean, about 6 Sv are flowing northward across 20°S, which when superimposed on the Mozambique Channel transport, produces a total of about 20 Sv flowing southward. Finally, the Antarctic Circumpolar Current (ACC) has a mean transport of 138 Sv, which south of Australia, is enhanced by the 14 Sv going around Australia in a time-average recirculation of the Indonesian Throughflow identified previously by *Macdonald and Wunsch* (1996) and consistent also with the *Ganachaud and Wunsch* (2000) results from later data. The estimate of the Indonesian Throughflow is in good agreement with estimates based on in situ data (*Gordon*, 1986; *Roemmich et al.*, 1996; *Godfrey*, 1996) and which were not used as constraints.

Fig. 4 shows time series of volume transports from the South Pacific across 36°S, and along the ACC south of Australia (with the large-scale ACC component through Drake Passage removed to demonstrate the local variability) and, with negative amplitude, the flow through the Indonesian Throughflow and the Indian Ocean across 36°S. The respective timeseries track each other. A seasonal cycle superimposed on the high-frequency fluctuations is apparent. The degree of agreement of the high-frequency variations across the Indo-Pacific basin is obvious from the inset that shows a one-year fraction of high- Fig. 4

pass filtered volume transport timeseries from the South Pacific and the southern Indian Ocean across 30° S—the latter plotted with opposite sign.

The time series in Fig. 4, the Mozambique Channel Throughflow minus that from the Indonesian Throughflow, compares very well with the transport moving north across the remaining Indian Ocean at 20°S. Apparently, there is a circulation system around Madagascar involving both the mean and the time-dependent circulations alike, and that affects, in separate loops, the Indian Ocean and the entire the Indo-Pacific system (*Godfrey*, 1996). High frequency fluctuations of about 10-15 Sv in the Mozambique Channel have a net standard deviation of about 5 Sv. The ACC south of Africa, Australia, and through Drake Passage, shows a strong seasonal cycle superimposed on high-frequency fluctuations. Near Australia, the additional, largely high-frequency variability seen in the Mozambique Channel characterizing the Indo-Pacific closed loop circulation, is superimposed on the ACC transport variability.

Various previous estimates of the ACC transport exist. For example, *Whitworth* (1983), using a combination of moorings and hydrographic surveys, estimated a range of 118-146 Sv, with a mean of 121 Sv through the Drake Passage, but subject to various sampling errors. Nowlin and Klink (1986) report 135 $\pm$ 5 Sv in good agreement with our results. As with the other sections, results for the ACC show that reports of "mean" volume transports from field programs of duration of a year or shorter cannot and should not be interpreted as representing the long-term average. In particular, the Indonesian Throughflow and Drake Passage fluxes would require many years of averaging to produce a stable mean (and the model underestimates the high frequency variability owing to the absence of eddies and related motions).

Fig. 4 shows that in the model, the South-Pacific Indian Ocean system is spinning down in the sense that the northward transport and its return in the Indian Ocean is weakening by almost 5 Sv. over the six years. At the same time the ACC transport is strengthening steadily over the entire period. Note also that the Indian Ocean shows almost no net northward volume flux during boreal winter, and a maximum of around 10

Sv between October and December.

Fig. 5a shows a spectral estimate of the transport across 20°S in the Pacific and compares it with a similar estimate from the Mozambique Channel minus the transport across the remaining Indian Ocean at this latitude. The results and their coherence (Fig. 5b) are consistent with the visual impression that the variations in both records are almost identical at periods longer than about fifty days at zero phase. (Fig. 5c). The causes of this large scale variation have not been established, but are conjectured to be a combination of directly forced large-scale wind-driven motions and a dominantly barotropic response. Such large scale motions demonstrate the connected nature of the ocean circulation and its variability, and underline the need to study it on a global basis. Fig. 5

Volume flux variability is of course, not uniformly distributed along the sections. As one example, Fig. 6 shows the logarithm of the standard deviation of volume flux along 31°S. High variability is associated primarily with shallow boundary currents on both sides of the Indian and Pacific Oceans. However, enhanced variability in the northward velocity component can also be seen along the flanks of most steep topographic features in the model, notably the Ninetyeast Ridge in the central Indian Ocean and the East-Pacific Rise. Note that the latter was previously identified as a region of vigorous barotropic variability (e.g., *Fukumori et al.* 1998; *Stammer et al.,* 2000). A similar feature appears in the Indian Ocean sector of the figure, although with reduced amplitude. Fig. 6

The trends in volume transport (Fig. 4) indicate a remaining overall mass adjustment occurring in the model. This adjustment is displayed in a more complete way in Fig. 7 showing the mean changes in sea surface height over the six year period. The largest changes are of the order of $\pm$ 20 cm and can be found over the subtropical gyres of the northern hemisphere. Smaller changes are visible across the model ACC. The associated mean southward volume flux is obtained by averaging the model meridional flow over the entire globe. Results are consistent with the changes in sea surface height and indicate adjustments of the order of 10^{-3} Sv. The values are approximately the same as seen in TOPEX/POSEIDON global and regional trend data (*Nerem et al.*, 1999; F. Condi personal communication, 2000) and demonstrate one of the difficulties encountered in Fig. 7

explaining global sealevel rise in the presence of numerical model drift.

3 Mean Heat and Freshwater Fluxes

The time rate of change of a heat content Q, defined in (1) is,

$$\frac{\partial Q}{\partial t} = -\nabla \cdot F_Q + H_Q, \tag{3}$$

where H_Q is the surface net heat flux and the zonally integrated meridional transports of temperature is

$$F_Q = \rho c_p \int_0^L \int_{-H}^0 v\theta dz dx. \tag{4}$$

(see *Bohren and Albrecht*, 1998 or *Warren*, 2000, for a discussion of the meaning of "heat transport", which we will nonetheless continue to use as a shorthand for "energy transport").

Time mean values of F_Q in the model across various WOCE sections and their standard deviation are shown in Fig. 4b. In the present solution, there is a mean temperature flux of about 1.3 PW from the Pacific into the Indian Ocean. Most of this heat then moves southward through the Mozambique Channel. In contrast to the volume flux, the entire Indian Ocean shows southward temperature flux at the latitude of Mozambique. Some of it is communicated to the atmosphere between 20°S and 36°S and about 1 PW is being released into the ACC region. Note that in our estimate, the 0.25 PW transported from the Indo-Pacific system into the Atlantic follows the "cold-water route" through the Drake Passage (see *Gordon*, 1986; *Rintoul*, 1991*Macdonald*, 1998; *Ganachaud and Wunsch*, 2000). This total dominance by the cold-water route may be a consequence of the absence of any eddy variability or Agulhas ring formation in the coarse-resolution model.

Fig. 8 shows zonally integrated meridional heat fluxes and separately for the Atlantic and Pacific-Indian Oceans. Also shown are error bars estimated as $\sigma/\sqrt{N}$ from the temporal standard deviations σ, with N being the number of degrees-of-freedom, taken

Fig. 8

here to be approximately 435—the number of individual 5-day estimates. The green open circles show the zonal integrals as obtained by *Ganachaud and Wunsch* (2000). Although our estimates agree with theirs surprisingly well in the Southern Hemisphere and in the North Pacific, large discrepancies exist over the Atlantic where we estimate only about 50% of their amplitude, except at 10°N and at the southern end of the picture. However, this result is unsurprising in a 2° lateral resolution model in which the boundary currents are sluggish and diffuse, with the data unable to impose a different, sharper, spatial structure. Despite this resolution problem, the gross pattern of North Atlantic poleward heat flux is reproduced and its dependence on the closed nature of the poleward model boundaries or other model parameters has to be investigated. See *Stammer et al.* (2001b) for a further discussion.

In Fig. 9 we show the zonally integrated meridional freshwater transports and their standard deviation, estimated as Fig. 9

$$F_W = \int \int_{-H}^{0} \rho v (1 - S) dz dx. \tag{5}$$

Freshwater flux estimates are in turn very similar to *Wijffels et al.* (1992) over most parts of the ocean.

Basin-integrated net surface heat and freshwater fluxes, corresponding to the divergences of the meridional fluxes in Figs. 8 and 9, are shown in Fig. 10 evaluated here from the estimated surface net heat and freshwater flux fields displayed in Paper 1. Both global integrals, and those for individual basins are shown. Heat flux in the Northern Hemisphere outside the tropics is negative, that is, the ocean loses heat to the atmosphere. A similar result appears in the Southern Hemisphere between 10° and 40°S. The Southern Ocean, however, shows a pronounced warming pattern with net amplitude close to 1/3 of that of the tropical ocean. This warming is mostly located over the Atlantic and Indian sectors of the ACC, again consistent with the *Ganachaud and Wunsch* (2000, their Fig. 1) results. Heat is lost by the ocean over the South Pacific and Indian Oceans, while the Atlantic shows a net heat gain over the southern hemisphere. Note the small heat gain Fig. 10

in the tropical Indian Ocean— indicating that most of the heat lost south of 10°S over that basin must be imported from the Pacific through the Indonesian Throughflow or the Southern Ocean.

For freshwater, we find a net gain (excess precipitation) over the tropics, but also at high latitudes, especially over the ACC. Losses are quite similar in pattern between Atlantic, Pacific and Indian Ocean, although the Indian Ocean shows enhanced evaporation around 40°S. The salinity maximum in North Atlantic and its origin in the strong freshwater loss over the eastern subtropical Atlantic is quite well known. Here a similar forcing effect also appears in each of the other sub-tropical gyres.

4 Kinematics of Transport Variations

Temporal variations of the meridional heat transports are large, especially in low latitudes where they can be many times larger than their mean values. But an estimate of the "eddy part" $\overline{v'\theta'}$ for the global average is as expected small and is not significant in this coarse-resolution computation. See the discussion, e.g., by *Böning and Bryan* (1996) and *Jayne and Marotzke* (2001) of computations with unconstrained eddy-permitting models .

Regional budgets of heat and their changes with time will be discussed in the next section. First however, we discuss the structure in the Atlantic of the temporal heat transport changes in our solution. In Fig. 11 is the split total heat transport there in various contributions originating from different parts of the water column. The figure shows temperature transport in various depth classes: (0-50m; 50-800, and below 800m), Fig. 11

$$H_q = \rho c_p \left(\int_{-50}^{0} v\theta dz + \int_{-800}^{-50} v\theta dz + \int_{-h}^{-800} v\theta dz \right). \tag{6}$$

Also shown is the heat transport split into temperature classes: ($\theta > 10$°C; 4°C $< \theta <$ 10°C; $\theta < 4$°C), so that,

$$H_q = \rho c_p \left(\int_{z(10^o)}^{0} v\theta dz + \int_{z(4^o)}^{z(10^o)} v\theta dz + \int_{-h}^{z(4^o)} v\theta dz \right). \tag{7}$$

The mean depths of the 10°C and 4°C isotherms are given in Fig. 12 for the global model domain together with a map of the 20° isotherm depth (compare Fig. 1). Gyre signatures are conspicuous, as are the source regions for water masses and ventilation "windows". Fig. 12

A summary of the overall result is that the largest part of the variability is associated with the shallow near-surface layers that are dominated by high frequency near-surface Ekman transports (compare *Jayne and Marotzke*, 2001). We note that the annual cycle increases towards the equator and that the high-frequency variations in temperature transports in the near-surface range are not compensated instantaneously by deeper compensating transports at most latitudes. Only at 47°N can significant compensation be seen, and during winter months alone. As a result, most of the corresponding heat must be stored locally and is then redistributed by the shallow layers. In contrast to the shallow regions, the deeper layers show more seasonal to interannual variations. Nevertheless, the shallow wind-driven variations also display interannual variations of amplitudes similar to the deeper part, especially in high latitudes as shown here for the North Atlantic. Note a clear upward trend in the temperature transport of the class $\theta > 10°$, while the next lower θ class decreases in its transport at 47°N indicating the warming of the deeper layers there on basin average.

While our estimates do show drifts in deep temperatures, especially in the North Atlantic and Southern Ocean, some of it may reflect actual ocean variability. *Levitus et al.* (2000) and *Barnett et al.* (2001) discuss the temperature increase in the ocean over the last decade as deduced from ocean data and from a coupled ocean-atmosphere numerical climate simulation. Both analyses show significant and comparable increases in deep temperature in both the North Atlantic Southern Oceans. Separating numerical drifts from climate related trends in the deep ocean will be a challenge for long-term climate simulations and estimations.

In Fig. 13 we show the time-mean volume and temperature transports analogous to Fig. 3b, but now separated by depth and temperature classes. The shallow nature of the Ekman cells is apparent—with high volume being transported in one direction near Fig. 13

the surface and returned in the next depth class. As a consequence of the shallow nature of the cell, its effect is basically averaged out in the temperature classes. Water warmer than 4°C moves northward in the Atlantic and colder water returns southward. Near the equator and north of it, water warmer than 10°C carries the entire northward volume flux.

Associated with the shallow overturning cell is a strong temperature transport, especially in the tropical oceans and over large regions of the Pacific Ocean. Note that most of the temperature transport variability occurs at temperatures above 10°C and that the temperature transports in the two lower temperature classes nearly compensate each other. In general terms, the Indian Ocean carries warm water southward, and which subsequently is returned northward in the Atlantic via the "coldwater" route through Drake Passage.

In the South Pacific, a northward flow has contributions from all temperature classes, but with the main component lying above 4°C. This water is returned southward in the Indian Ocean—generally above 10°C. In the North Pacific, each temperature class seems to be balanced in terms of its volume flux, and no largescale net temperature flux is apparent.

There also exists (not shown) a significant seasonal cycle in the temperature flux along the ACC south of the Cape of Good Hope with vigorous short-period variations superimposed. Across Drake Passage, the transports are much more stable and vary mostly in a small amplitude seasonal cycle. In contrast, south of Australia no visible seasonal cycle appears, and temperature flux variations have much of the character of the volume fluxes (Fig. 4).

To investigate the various components present, we write the transport across each of the sections in the form

$$H_q(t) = \int_0^L \int_{-H}^0 \overline{v}\,\overline{\theta} dz dx + \int_0^L \int_{-H}^0 v'(t)\theta'(t) dz dx + \int_0^L \int_{-H}^0 \overline{\theta} v'(t) dz dx + \int_0^L \int_{-H}^0 \overline{v}\,\theta'(t) dz dx \tag{8}$$

where integrals are being taken along zonal sections and where the bar indicates the time-

average. The decomposition is shown in Fig. 14 (except the first right-hand term). The last term, in θ', gains importance towards high latitudes and is responsible for almost all seasonal changes there. Note that both terms involving v' tend to be of opposite sign at mid- and high latitudes during all winter seasons (i.e. in winter time enhanced meridional flow carries colder water), and are in phase during summer. Towards low latitudes, most of the variability is in the $v'\overline{T}$ term, while the two other terms are very small. In summary, accurate flow estimates are the most important information for estimating the time-varying temperature transports in low latitudes, while at high latitudes both the changing flow and temperature fields must be known. Fig. 14

Another way to look at the temperature/heat fluxes is to separate their contributions to the vertical overturning from that of the horizontal gyre effect, or equivalently the vertical mean contribution from the vertically varying one. To do so, define $\tilde{V}(z,t)$ as the zonal average of $V(x,z,t)$, $\tilde{V}(x,z,t)' = V(x,z,t) - \tilde{V}(z,t)$ and V_d as the vertical average and $V_d'(x,z,t) = V(x,z,t) - V_d$. Then the heat flux can be written as (see also *Böning and Bryan*, 1996)

$$F_q = \rho c_p \int_0^L h(x) V_d T_d dx + \int_0^L \int_{-h(x)}^0 V_d' T_d' dz dx = F_0 + F_1, \tag{9}$$

i.e., split into a depth independent, and depth-dependent components. (Note that purely baroclinic flows produce non-zero vertical average volume fluxes, and it would be incorrect to call F_0 the "barotropic" component.) $h(x)$ is the water depth. Equivalently, we can write,

$$F_q = \rho c_p \left(\int_0^L \int_{-h(x)}^0 \tilde{V}\tilde{T} dz dx + \int_0^L \int_{-h(x)}^0 \tilde{V}'\tilde{T}' dz dx \right) = F_{OT} + F_G, \tag{10}$$

i.e., divided into overturning and gyre components. Further sub-decomposition is possible and these decompositions are not unique.

Several surprising results are visible from the four F_j terms shown in Fig. 14 as zonal integrals. High frequency changes in F_0 and F_{OT} are almost identical and dominate the

variability. As discussed in *Jayne and Marotzke* (2001), this variability arises from the variable Ekman transport and a true barotropic return flow. At 47°N however, F_0 and F_{OT} show different secular trends. Although smaller in amplitude, F_0 and F_G are significant, with the latter slowly decreasing in amplitude over time except at high frequencies. Near the equator, F_0 becomes almost white noise, but F_G shows an interesting seasonal cycle. Further south, F_0 becomes more significant, with F_G becoming very small.

Fig. 15 shows time mean values of F_j as a function of latitude for the global ocean and separately for the Atlantic and Indo-Pacific sectors. Surprisingly, around 25°N, F_0 is the dominant transport mechanism on the global average. Towards higher latitudes, all F_j become small, but equatorwards, F_1 and F_{OT} dominate. (The reader is reminded that these are not additive contributions.) Fig. 15

In the Indo-Pacific F_0 is large in the northern hemisphere and south of the equator, and largely compensated by F_1 north of the equator. In the Atlantic, F_1 or F_{OT} dominate, but around 25°N, F_0 is enhanced, while F_G grows south of the equator. A comparison with Fig. 4.11 and 4.12 in *Böning and Bryan* (1996) shows that our results are almost identical to theirs in terms of the general structure, especially for the overturning component from the 1/3° CME results. But our gyre component is somewhat smaller than their result from a 1° model version of the North Atlantic. In agreement with the present results, the CME shows an enhanced F_0, although it is slightly further north, near 30°N. The basic difference is that we obtain only a small fraction of their depth-independent amplitude—with more than 1 PW carried there in the CME result.

Fig. 16 displays zonal sections of the time-mean $\overline{vT}$ as a function of longitude and depth. Note the similar structures of temperature transports in the Pacific and Atlantic, including the negative (southward) flux at the western boundary owing to similar, but weaker and more shallow a deep western boundary current in the Pacific Ocean. The standard deviation of vT is almost the same as that of $v'\overline{T}$. Note the substantial fluctuations in mid-depth, especially near all western and eastern boundaries, but also over pronounced topographic features. This variability originates from strong first mode Rossby waves, Fig. 16

some of which originate at the eastern boundary and propagate westward interacting with the mid-ocean ridges (*Herrmann and Krauss,* 1989)

Fig.17 displays similar fields, but for the Southern Hemisphere along 21°S. Note the second-mode structures of the temperature transports and their variances in almost all western and eastern boundary currents at this latitude. Highest variations in transports are generally located at the transition in the mean transports from positive to negative. Note also the large southward transports on both sides of Madagascar, which extends over a large fraction of the entire water column. Fig. 17

5 Global and Regional Heat Balances

An important question concerns the way in which the ocean transports and stores heat and how it communicates any regionally imbalanced heat flux through the surface to the atmosphere. Consider the heat content changes in various regions of the Pacific Ocean as shown in Fig. 18 . Area 1 includes the Kuroshio Extension in the North Pacific. Zonal and meridional horizontal transport divergences as well as their net contribution to the temperatures fluxed into the region are displayed in the upper panel of Fig. 19. The net lateral influx is clearly positive, indicating that the region is being supplied by heat from the ocean; in a steady state the excess must be released to the atmosphere. Fig. 18 Fig. 19

In the middle panel of the same column, we show again the net horizontal temperature flux divergence, together with the net surface heat flux of the same region and the net oceanic heat content change dQ/dt. The net oceanic heat influx is balanced by a net surface heat flux over that region of -8.8 W/m^2 leading to a almost stable heat content that varies only on the seasonal cycle (bottom panel).

Further to the east (Region II) the situation is somewhat different. Here the heat content is steadily rising over the six-year integration period. It was shown in Fig. 2 that XBT observations are consistent with this heat content increase (compare also *Barnett et al.*, 2001). Convergence of the horizontal fluxes is positive zonally and negative meridionally. The net effect is slightly positive over the first part of the period, but turns negative

subsequently, i.e., the ocean then carries heat out of this region. Net surface heat flux is also positive (6.6 W/m^2) and the heat content increase here can now be identified as a joint effect of horizontal transport convergence and surface flux during the first few years. The transport divergence subsequently halts and reverses the trend in the heat content. This is a good example showing that, although small in amplitude, oceanic transports and convergences, accumulate over long periods to produce substantial effects.

Region III and IV are located at the western and eastern side of the tropical Pacific, respectively (Fig. 20). Horizontal flux convergences are large here and show signs of ENSO effects, especially at the western side at the end of the period when the zonal convergence is markedly positive. At the eastern side, the zonal convergence is negative during 1997, but the meridional convergence becomes positive at almost the same rate, giving rise to only a small net negative transport convergence here. Note that in both regions, temporal changes in the oceanic heat content are dominated by the horizontal advection of temperature in and out of the regions. Fig. 20

Region V covers the area of the East Australia current (Fig. 21). There, the ocean flow changes markedly with the seasonal cycle. Boreal winters lead to net inflow of temperature and the flux is reversed six months later. The changes in the oceans net heat contents are somewhat smaller than the net surface heat flux fields would suggest and heat content variations on seasonal and interannual timescale are dominated by variations in horizontal flux divergences. Fig. 21

Finally, Region VI is located at the eastern side of the subtropical South Pacific. Note that the southern edge is influenced by enhanced high frequency wind-driven barotropic variability as documented, e.g., by *Fukumori at el.* (1998) and *Stammer et al.* (2000) (compare also Fig. 6). Meridional transport convergences are accordingly quite vigorous at high-frequencies, but to some extent are balanced by the zonal convergences and net effects are smaller than were seen on the western side. So again, the surface heat flux dominates the variability of net oceanic heat content changes, although longer-period variations due to changing ocean currents do exist.

6 Summary and Conclusions

A dynamically consistent time-dependent combination of a GCM and global data has been used to estimate ocean transports of volume, heat and fresh water and to analyse their temporal changes. Emphasis was put especially on an estimate of global oceanic cycles of heat storage and heat flux quantities of significant climate relevance. Because the quality of the underlying flow estimates is limited by the present low resolution, the most important results here are the demonstration that these computations are feasible. The estimates will gradually improve through the addition of new data, more complete model physics and higher resolution, but the present solution is probably among the best that can be done today. In particular, the analysis of the temporal variability of the flux properties is believed to be accurate except for the variability owing to the unresolved eddy field.

An important result from this study is that time-average fluxes estimated from this fully time-dependent circulation have converged with independent steady-flow estimates from box inversions over most parts of the world ocean but especially in the southern hemisphere. This was previously not the case; instead full assimilation attempts based on GCMs usually differed significantly from those based on simplified box inversions with more confidence being put into the latter as has been discussed in detail by *Marotzke and Willebrand* (1996). However, transport estimates still differ substantially in the North Atlantic where our estimates result in only 1/2 previous heat transports.

Although the low model resolution causes problems with estimates of the time average proprty fluxes, the patterns in the means are in encouraging quantitative agreement with the independent estimates of *Ganachaud and Wunsch* (2000). Equally important, we obtain an estimate of the ocean state that is basically in balance with simultaneous estimates of surface fluxes of momentum, heat and freshwater flux. The meridional heat transports estimated from both transports within the model and from integrals of the surface heat fluxes are mostly consistent with the exception of the North Atlantic and within error bars of Trenberth et al. (2001), in a comparison of NCEP, ECMWF, and COADS-derived

values. A more complete discussion is provided in *Stammer et al.* (2001b).

Mean and time-varying volume fluxes for the entire three dimensional ocean circulation are estimated. Among the more striking results are the confirmation of previous findings of a mean circulation around Australia which involves a net volume flux of 14 Sv through the Indonesian Throughflow and the Mozambique Channel. In addition, we show that this flow regime exist on all time scales longer than one month rendering the variability in the South Pacific strongly coupled to the Indian Ocean. Accordingly, the ACC shows a superposition of those regional flow changes to the global transports around Antarctica that are dominated by a seasonal cycle. An estimated mean ACC transport of 138 Sv is in good agreement with previous observational findings.

The temporal variability of oceanic heat flux, heat storage and atmospheric exchanges is complex, showing a dependence upon location, depth, and time-scale as described above. Oceanic transports, storage, and air/sea exchange follow a complicated geographical pattern and exhibit variability on all accessible time scales. For the first time, we now have a prototype ocean data synthesis tool that provides a quantitative ocean transport analysis.

The description given here of the oceanic heat budget remains tentative owing to remaining model/data shortcomings already described. However, we anticipate rapid improvement in all of the elements of the budget through model and data improvements now underway. Ongoing computations will complete a WOCE data synthesis including, in addition to the data used here, the WOCE hydrography, global XBT data sets, TOA temperature measurements, drifter surface velocities, etc. Computations are being carried out now on a nominal 1 $^\circ$ grid and include mixed layer dynamics. These and related computations will likely be the pattern for future design and synthesis of all future large-scale observation programs.

Acknowledgments. Computational support from the National Partnership for Computational Infrastructure (NPACI) and the National Center for Atmospheric Research (NCAR) is acknowledged. Supported in part through ONR (NOPP) ECCO grants N00014-99-1-1049 and N00014-99-1-1050, through NASA grant NAG5-7857, through NSF grant OCE 9730071 and through two contracts with the Jet Propulsion Laboratory (958125 and 1205624).

References

[1] Barnett, T., D.W. Pierce and R. Schnur, 2001: Detection of anthropogenic climate change in the world's ocean. *Science*, 292, 270–274.

[2] C. F. Bohren and B. A. Albrecht, *Atmospheric Thermodynamics*, Oxford Un. Press, New York, 1998, 402 pp.

[3] Böning, C.W., and F.O. Bryan, 1996: Large-scale transport processes in high-resolution circulation models. In: *The Warmwassersphere of the North Atlantic.* W. Krauss (ed.), Gebr. Bornträger, Stuttgart, pp. 91-128.

[4] Carton, J.A., G. Chepurin, X. Cao, and B.S. Giese, 2000a: A Simple Ocean Data Assimilation analysis of the global upper ocean 1950-1995, Part 1: methodology, *J. Phys. Oceanogr.*, 30, 294-309.

[5] Carton, J.A., G. Chepurin, and X. Cao, 2000b: A Simple Ocean Data Assimilation analysis of the global upper ocean 1950-1995 Part 2: results, *J. Phys. Oceanogr.*, 30, 311-326.

[6] Fukumori, I., R. Raghunath, and L.-L. Fu, 1998: Nature of global large-scale sea level variability in relation to atmospheric forcing: a modeling study, *J. Geophys. Res., 103*, 5493-5512.

[7] Ganachaud, A. and C. Wunsch, 2000: Oceanic meridional overturning circulation, mixing, bottom water formation rates and heat transport. Nature, 408, 453-456.

[8] Garnier, E., B. Barnier, L. Siefridt and K. Béranger, 2001: Investigating the 15 years air-sea flux climatology from the ECMWF reanalysis project as a surface boundary condition for ocean models. *International Journal of Climatology*, submitted for publications.

[9] Gordon, A.L., 1986: Interocean exchange of thermocline water. *J. Geophys. Res.*, 91, 5037–5046.

[10] Godfrey, J.S., 1996: The effect of the Indonesian throughflow on ocean circulation and heat exchange with the atmosphere: A review. *J. geophys. Res.*, 101, 12,217–12,2238.

[11] Herrmann, P. and W. Krauss, 1998: Generation and propagation of annual Rossby waves in the North Atlantic. *J. Phys. Oceanogr.*, 19, 727–744.

[12] Jayne, S.R. and J. Marotzke, 2001: The dynamics of ocean heat transport variability. *Rev. Geophys.*, 39, 385–412.

[13] Josey, S.A., E.C. Kent and P.K. Taylor, 1999: New insight into the ocean heat budget closure problem from analysis of the SOC air-sea flux climatology. *J. Clim.*, 12, 2856–2880.

[14] Lemoine, F. and 17 others The development of the NASA GSFC and NIMA Joint Geopotential Model. in, *Proceedings of the International Symposium on Gravity*, Geoid and Marine Geodesy, IAG Symposium: in press H. Fujimoto, ed. Springer-Verlag.

[15] Levitus, S., J.I. Antonov, J. Wang, T.L. Delworth, K.W. Dixon and A.J. Broccoli, 2000: Anthropogenic warming of Earth's climate system. *Science*, ???.

[16] Levitus, S., R. Burgett, and T. Boyer, *World Ocean Atlas 1994*, vol. 3, *Salinity*, and Vol. 4, *Temperature*, *NOAA Atlas NESDIS 3 & 4*, U.S. Dep. of Comm., Washington, D.C., 1994.

[17] Macdonald, A.M., The global ocean circulation: a hydrographic estimate and regional analysis. *Prog. Oceanography*, 41, 281–382, 1998.

[18] Macdonald, A.M., and C. Wunsch, An estimate of global ocean circulation and heat fluxes, *Nature,* 382, 436-439, 1996.

[19] Marotzke, J., J. Willebrand, 1996: The North Atlantic mean circulation: combining data and dynamics. In *Warm Water Sphere of the North Atlantic Ocean*, edited by W. Krauss, Gebrüder Bornträger, Berlin, 159–193.

[20] Marshall, J., A. Adcroft, C. Hill, L. Perelman, and C. Heisey, A finite-volume, incompressible navier-stokes model for studies of the ocean on parallel computers. *J. Geophys. Res.* , 5753–5766, 1997.

[21] McPhaden MJ, Busalacchi AJ, Cheney R, Donguy JR, Gage KS, Halpern D, Ji M, Julian P, Meyers G, Mitchum GT, Niiler PP, Picaut J, Reynolds RW, Smith N, Takeuchi K, 1998: The tropical ocean global atmosphere observing system: A decade of progress. *J. of Geophys. Res.*, 103, 14169-14240.

[22] Nerem, R.S., D.P. Chambers, E.W. Leuliette, G.T. Mitchum, B.S. Giese, 1999: Variations in global mean sea level associated with the 1997-1998 ENSO event: Implications for measuring long term sea level change *Geophys. Res. Lett.*, 26, 3005-3008.

[23] Nowlin, Jr., W.D., and J.M. Klink, 1986: The physics of the Antarctic Circumpolar Current. *Rev. Geophys. Space Phys.*, 24, 469–491.

[24] Ponte, R., D. Stammer and C. Wunsch, 2001: Improved ocean angular momentum estimates using an ocean model constrained by large-scale data, *Geoph. Res. Letters*, in press.

[25] Rintoul, S., 1991 South Atlantic inter-basin exchange. *J. Geophys. Res.,* 96, 2675-2692.

[26] Roach, A.T, K. Aagaard, C.H. Pease, S.A. Salo, T. Weingartner, V. Pavlov, and M. Kulakov, 1995: Direct measurements of transport and water properties through the Bering Strait, *J. Geophys. Res.*, 100, 18,443-18,457.

[27] Roemmich, D., S. Hautala and D. Rudnick, 1996: Northward abyssal transport through Samoan Passage and adjacent regions. *J. Geophys. res.*, 101, 14039–14055.

[28] Stammer, D., C. Wunsch, and R. Ponte, 2000: De-aliasing of global high frequency barotropic motions in altimeter observations, *Geophysical Res. Letters*, 27, 1175-1178.

[29] Stammer, D., C. Wunsch, R. Giering, C. Eckert, P. Heimbach, J. Marotzke, A. Adcroft, C.N. Hill, and J. Marshall, 2001, The global ocean circulation during 1992 –1997, estimated from ocean observations and a general circulation model, submitted for publication.

[30] Stammer, D., K. Ueyoshi, W. Large and C. Wunsch, 2001b: Surface Fluxes Estimated Through Ocean Data Assimilation, to be submitted.

[31] Tierney, C., J. Wahr, F. Bryan and V. Zlotnicki, 2000: Short-period oceanic circulation: implications for satellite altimetry. Geophys. res. Letters, 27, 1255–1258.

[32] Trenberth,.K. E., J. M. Caron and D. P. Sepaniak. The atmospheric energy budget and implications for surfaces fluxes and ocean heat transports. *Clim. Dyn.,* 17, 259-276, 2001.

[33] Warren, B. A. Approximating the energy transport across oceanic sections *J. Geophys Res.*, 104, 7915-7919, 1999.

[34] Whitworth, T, Monitoring the transport of the Antarctic Circumpolar Current at Drake Passage. *J. Geophys. Res.,* 13, 2045-2057, 1983.

[35] Wijffels, S.E., R.W. Schmitt, H. Bryden and A. Stigebrand, 1992: Transport of freshwater by the ocean. *J. Phys. Oceanogr.*, 22, 155-162.

Figure Captions

Fig. 1: (top) Depth of 20° isotherm as a function of time evaluated from TOGA TAO data from 140° to 150° E on the equator (blue dots). Red and green dots are estimates at the same location obtained from the unconstrained and constrained model runs, respectively. (middle) Same as top panel, but from 265° E on the equator. (bottom) Zonal difference in the depth of the 20° isotherm, evaluated from the unconstrained (blue) and constrained model (red), respectively.

Fig. 2: Heat content (Joules) estimated over 20°x20° regions centered at 190°E, 30°N and 150°E, 10°S. Red lines are the results from the unconstrained model. Blue lines show results from XBTs, and the green lines are results from the constrained model.

Fig. 3: (top) Mean and standard deviations of volume flux (Sv) across sections as shown. (bottom) Mean and standard deviations of temperature transports (converted to Petawatts, PW) across various sections .

Fig. 4: Top panel: Time series of volume transports from the South Pacific across 36°S (green); along the ACC south of Australia (red) with the large-scale ACC component through Drake Passage removed. Negative values are from the the Indonesian Throughflow (blue curve) and the Indian Ocean across 36°S (magenta). Right inset shows a short segment of the high-pass filtered timeseries in the Pacific Ocean (blue) and across the Madagascar Channel (red, with opposite sign). Middle panel: Time series of the Mozambique Channel Throughflow minus that through the Indonesian Throughflow (red curve) and the transport going north across the remaining Indian Ocean at 20°S (blue curve). Bottom panel: The ACC transports south of Africa, Australia, and and through Drake Passage shown as blue, green and red curves, respectively.

Fig. 5: (a) Power spectral density of volume flux time series from 21°S across the South Pacific (solid curve) and across the Mozambique Channel minus the Indian Ocean at that location (dashed curve). (b) Coherence amplitude for the two timeseries shown in (a). (c) Coherence phase for the two time series with the sign of the Madagascar Channel transport reversed for display purposes.

Fig. 6: $\log_{10}$ of the standard deviation of meridional velocity v as a function of depth and longitude along 31°S across the Pacific and Indian Ocean.

Fig. 7: (top) Mean sea surface height changes over the six year simulation period estimated from a least-squares fit procedure. Contour interval is 5 cm. (bottom) Time-mean meridional volume transports (SV) integrated zonally acoss the entire model domain.

Fig. 8: Top panel: Integrated time-mean meridional heat transports for the global ocean estimated for various zonal sections in the model (blue curve). The blue error bars are estimated as $\sigma/\sqrt{N}$ where σ is the standard deviation in time of those fluxes, evaluated over the 5 year period every 5 days and $N = 435$, assuming individual estimates are independent. The green error bars mark the standard deviation obtained from individual annual mean estimates. The red curve represents the ocean heat transport inferred from estimated surface heat fluxes. Middle and bottom panels: Estimated meridional heat transport across zonal section sin the model, evaluated separately for the Atlantic, Pacific-Indian Oceans. All red symbols represent estimates from *Ganachaud and Wunsch* (2000) at the respective latitudes and their formal uncertainties.

Fig. 9: Top panel: Integrated time-mean meridional fresh water transports (in kg/s) for the global ocean estimated from zonal sections in the model. Blue error bars are

estimated similar to those for heat fluxes. The green error bars mark the standard deviation obtained from individual annual mean estimates. Red symbols represent estimates from *Wijffels et al* (1992) at the respective latitudes. Middle and bottom panels: Estimated meridional fresh water transport across zonal section in the model, evaluated separately for the Atlantic, Pacific-Indian Oceans.

Fig. 10: Zonally integrated heat (top in W) and and surface fresh water fluxes (bottom in Kg/s), evaluated globally (blue curves) and over the Atlantic (red), Pacific (green) and Indian Ocean (magenta) sectors, respectively.

Fig. 11: Timeseries of temperature transports across several latitude circles in the Atlantic as indicated in the panels. The left column shows those transports evaluated over the depth classes (0-50m) (blue), (50-800m) (green) and (800 - bottom) (red). The right column similar transports are shown but evaluated over temperature classes (>10°C) (green), (10°C $> \theta >$ 4°C) (red) and (< 4°C) (light blue). The blue curve shows the total temperature transport.

Fig. 12: (top) Mean depths of (top) the 20°C isotherm, (middle) the 10°C isotherm and (bottom) the 4°C Isotherm. In meters.

Fig. 13: Maps of the mean volume (top) and temperature (bottom) transports. The left column shows results for depth classes, while the right column shows similar results for temperature classes.

Fig. 14: (left) Timeseries $H_Q(t) = \int\int v\theta dzdx$ (green curves) across zonal sections with locations given in the panels. Also shown are $\int\int v'\theta' dzdx$, $\int\int \overline{\theta} v' dzdx$ and $\int\int \overline{v}\theta' dzdx$ as blue, red and magenta lines, respectively. (right) Temperature transport time series evaluated as contributions from the overturning (OT; blue), the gyre (GY; green), the barotropic (BT, red) and baroclininc circulation (BC, light blue), respectively. See text

for details.

Fig. 15: (a) Zonally integrated heat transports resulting from the overturning (OT; blue), the gyre (GY; green), the barotropic (BT, magenta) and baroclininc circulation (BC, red), respectively. The middle and lower panels show similar results but separately for the Atlantic and Indian-Pacific sectors.

Fig. 16: Zonal sections of the time-mean $\overline{vT}$ as a function of longitude and depth along 25°N. The lower two panels show the standard deviation of vT which is almost the same as $v'\overline{T}$.

Fig. 17: Zonal sections of the time-mean $\overline{vT}$ as a function of longitude and depth along 21°S. The lower two panels show the standard deviation of vT which is almost the same as $v'\overline{T}$.

Fig. 18: Map showing regions 1 - 6 for which the heat content budget is shown in Figs. 19 - 21.

Fig. 19: (top) Horizontal temperature flux divergence in area 1 (left) and area 2 (right), plotted separately for the zonal contributions (red), the meridional contributions (green) and the net convergence (blue). (middle) Horizontal temperature flux convergence (green), net surface heat flux (red) and time-rate of change of heat content in the area (blue). (bottom) Timeseries of heat content (blue), integrated surface heat flux (red) and integrated horizontal convergence (green).

Fig. 20: Same as in Fig. 19, but for areas 3 and 4.

Fig. 21: Same as in Fig. 19, but for areas 5 and 6.

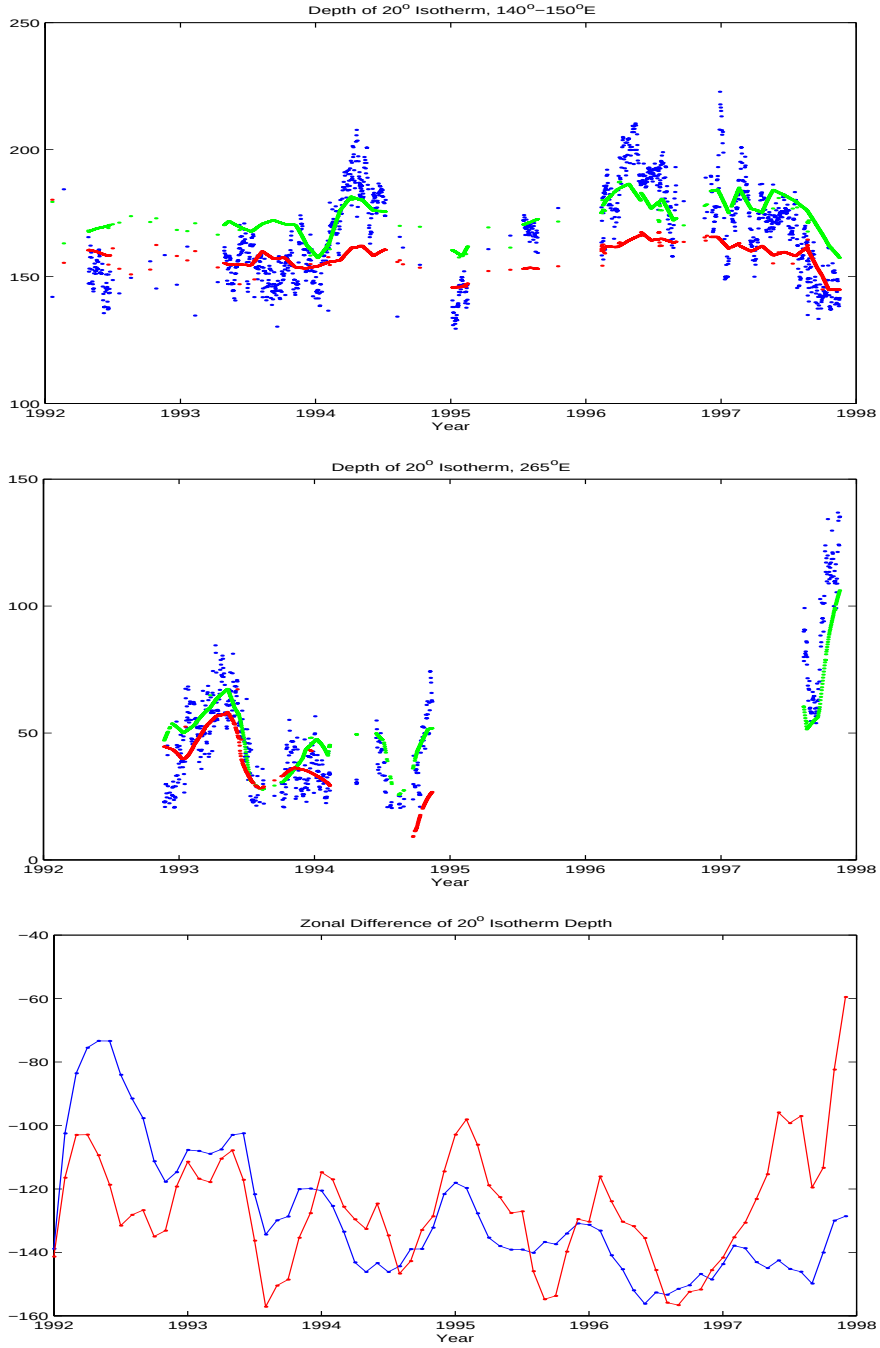
Depth of 20° Isotherm, 140°–150°E
250
200
150
100
1992
1993
1994
1995
1996
1997
1998
Year
Depth of 20° Isotherm, 265°E
150
100
50
0
1992
1993
1994
1995
1996
1997
1998
Year
Zonal Difference of 20° Isotherm Depth
−40
−60
−80
−100
−120
−140
−160
1992
1993
1994
1995
1996
1997
1998
Year

Figure 1:

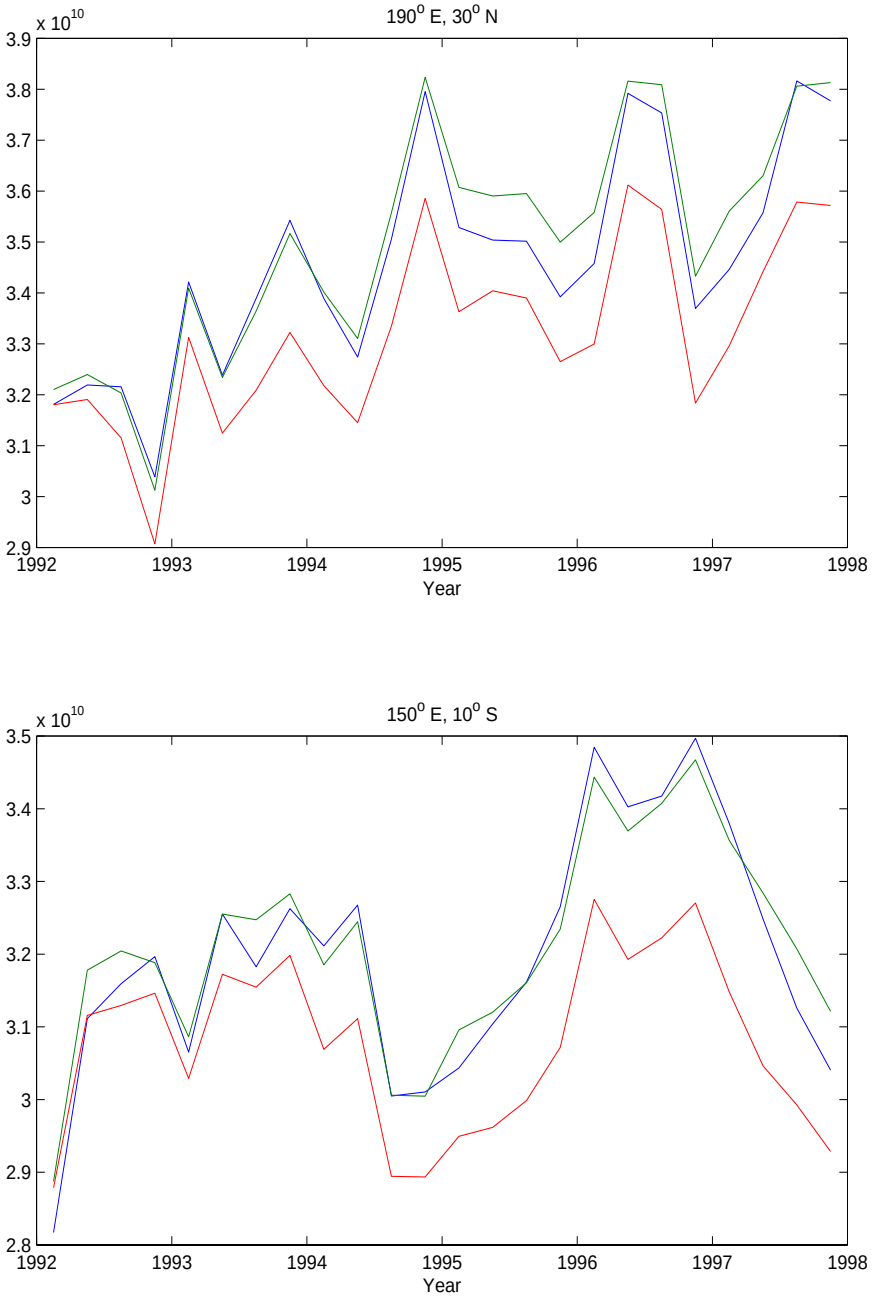
x 10^10
190° E, 30° N
3.9
3.8
3.7
3.6
3.5
3.4
3.3
3.2
3.1
3
2.9
1992
1993
1994
1995
1996
1997
1998
Year
x 10^10
150° E, 10° S
3.5
3.4
3.3
3.2
3.1
3
2.9
2.8
1992
1993
1994
1995
1996
1997
1998
Year

Figure 2:

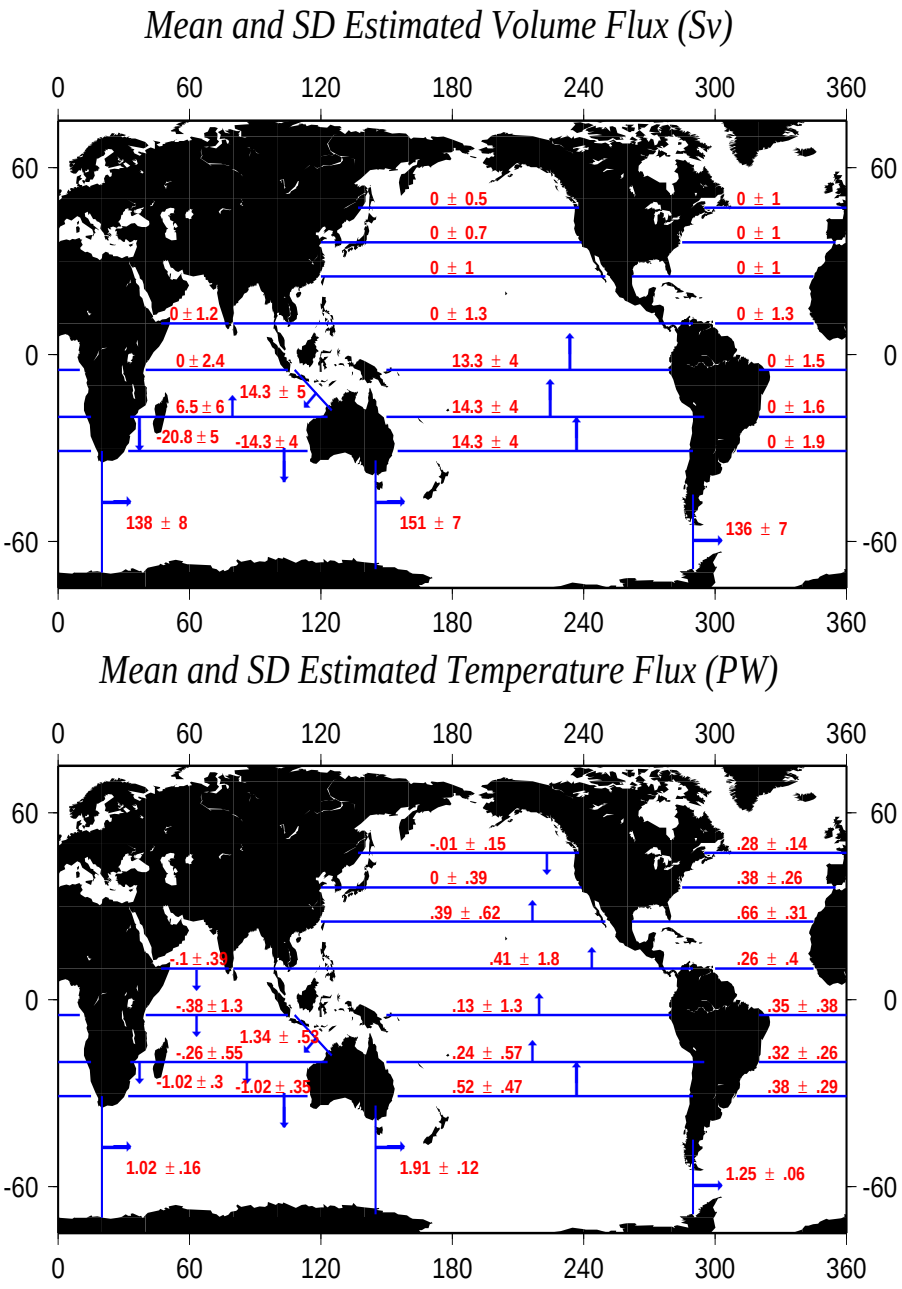
Mean and SD Estimated Volume Flux (Sv)
0 ± 0.5
0 ± 0.7
0 ± 1
0 ± 1.2
0 ± 2.4
6.5 ± 6
-20.8 ± 5
14.3 ± 5
-14.3 ± 4
138 ± 8
151 ± 7
0 ± 1
0 ± 1
0 ± 1
0 ± 1.3
13.3 ± 4
14.3 ± 4
14.3 ± 4
0 ± 1.3
0 ± 1.5
0 ± 1.6
0 ± 1.9
136 ± 7
Mean and SD Estimated Temperature Flux (PW)
-.01 ± .15
0 ± .39
.39 ± .62
-.1 ± .39
-.38 ± 1.3
-.26 ± .55
-1.02 ± .3
1.34 ± .52
-1.02 ± .35
1.02 ± .16
1.91 ± .12
.41 ± 1.8
.13 ± 1.3
.24 ± .57
.52 ± .47
.28 ± .14
.38 ± .26
.66 ± .31
.26 ± .4
.35 ± .38
.32 ± .26
.38 ± .29
1.25 ± .06
0
60
120
180
240
300
360
-60

Figure 3:

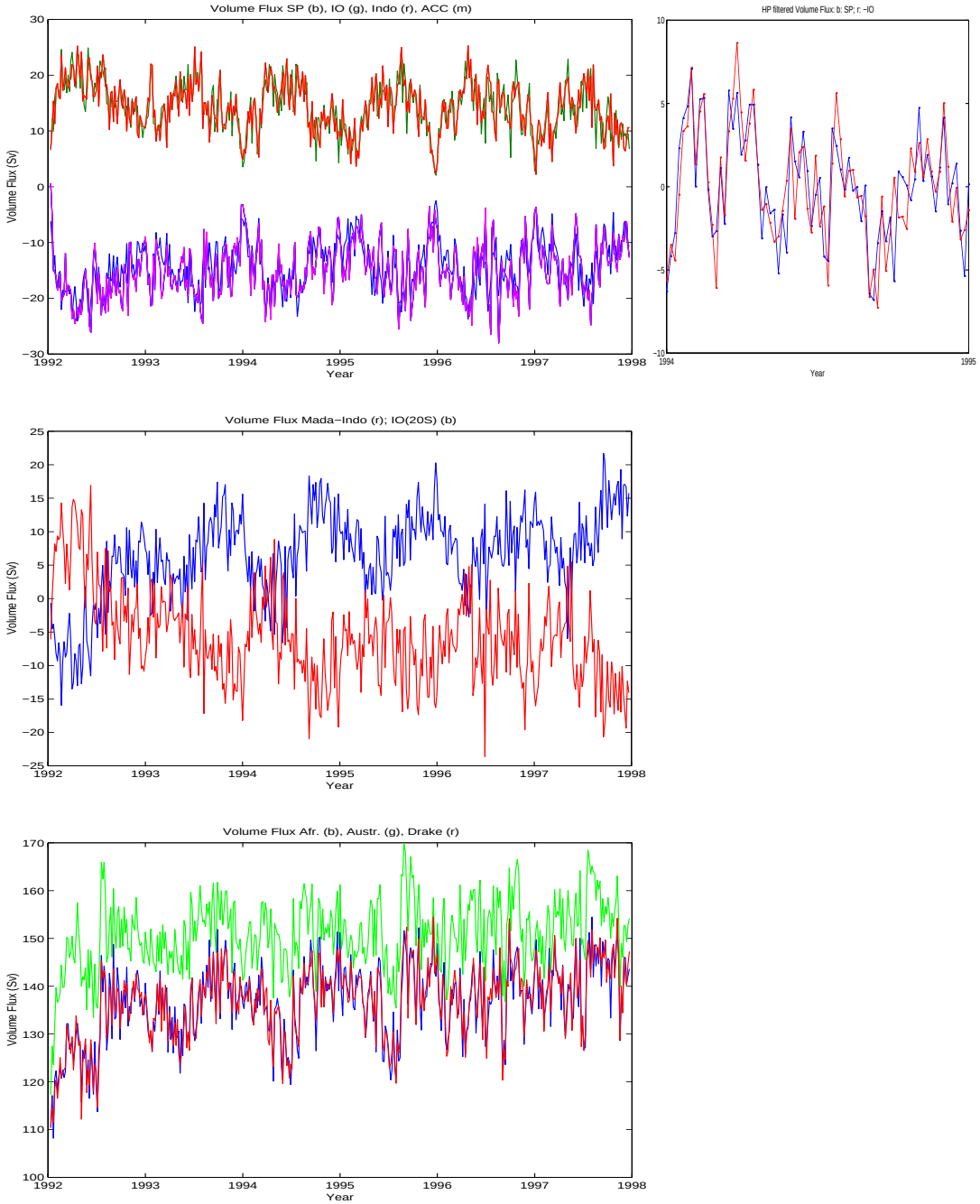
Volume Flux SP (b), IO (g), Indo (r), ACC (m)
Volume Flux (Sv)
Year
HP filtered Volume Flux: b: SP; r: −IO
Year
Volume Flux Mada−Indo (r); IO(20S) (b)
Volume Flux (Sv)
Year
Volume Flux Afr. (b), Austr. (g), Drake (r)
Volume Flux (Sv)
Year

Figure 4:

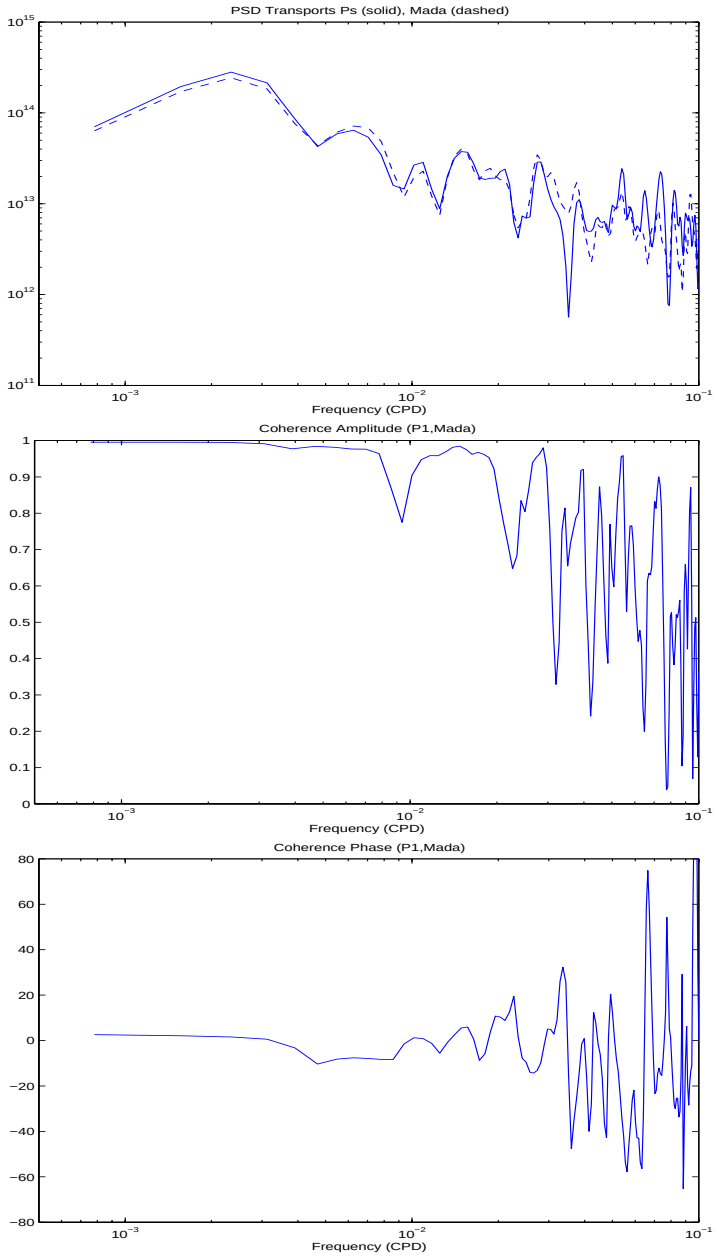
PSD Transports Ps (solid), Mada (dashed)
Frequency (CPD)
Coherence Amplitude (P1,Mada)
Frequency (CPD)
Coherence Phase (P1,Mada)
Frequency (CPD)

Figure 5:

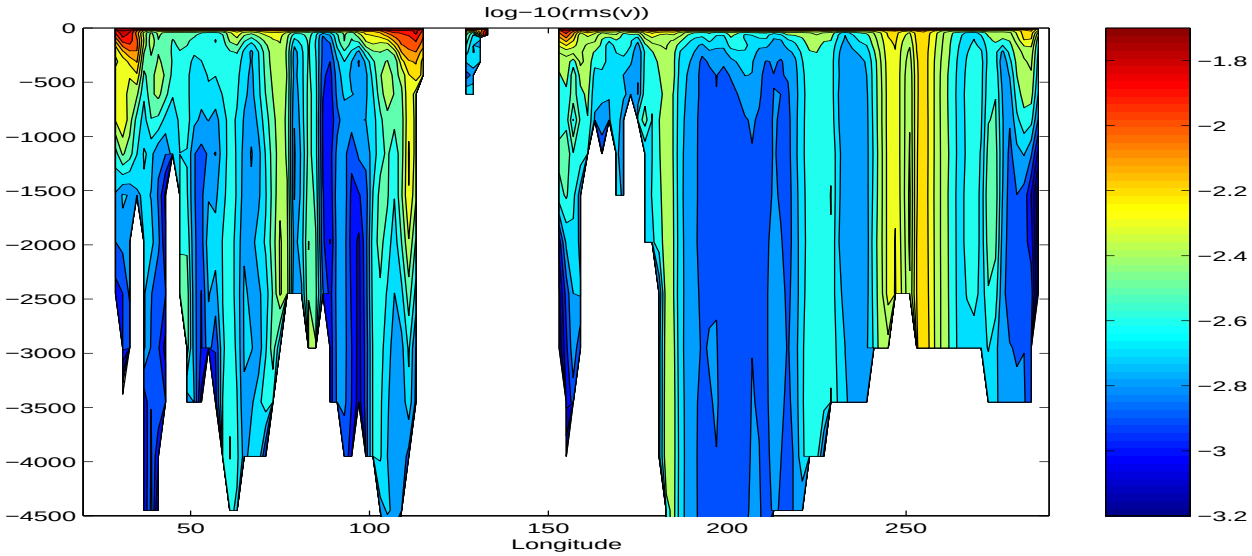
log−10(rms(v))
0
−500
−1000
−1500
−2000
−2500
−3000
−3500
−4000
−4500
50
100
150
200
250
Longitude
−1.8
−2
−2.2
−2.4
−2.6
−2.8
−3
−3.2

Figure 6:

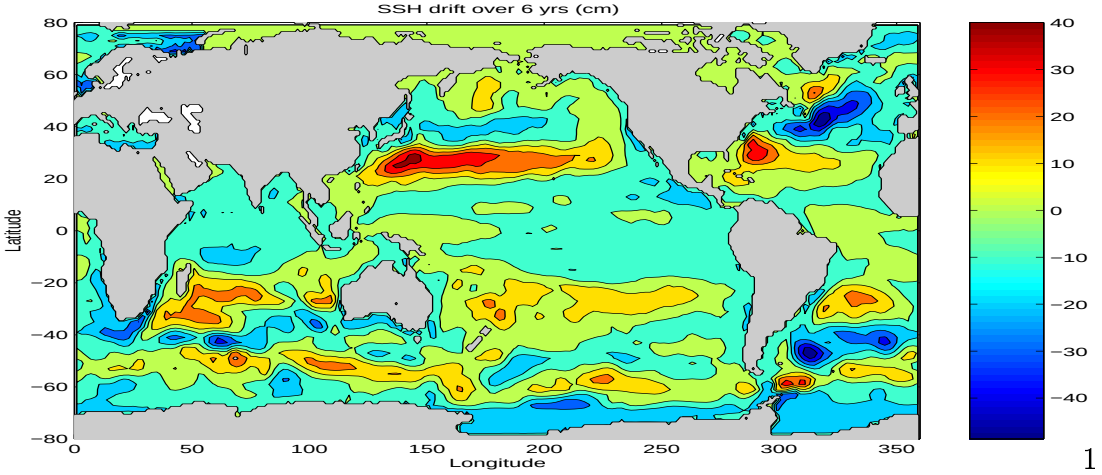
SSH drift over 6 yrs (cm)
Latitude
Longitude
80
60
40
20
0
−20
−40
−60
−80
0
50
100
150
200
250
300
350
40
30
20
10
0
−10
−20
−30
−40

1

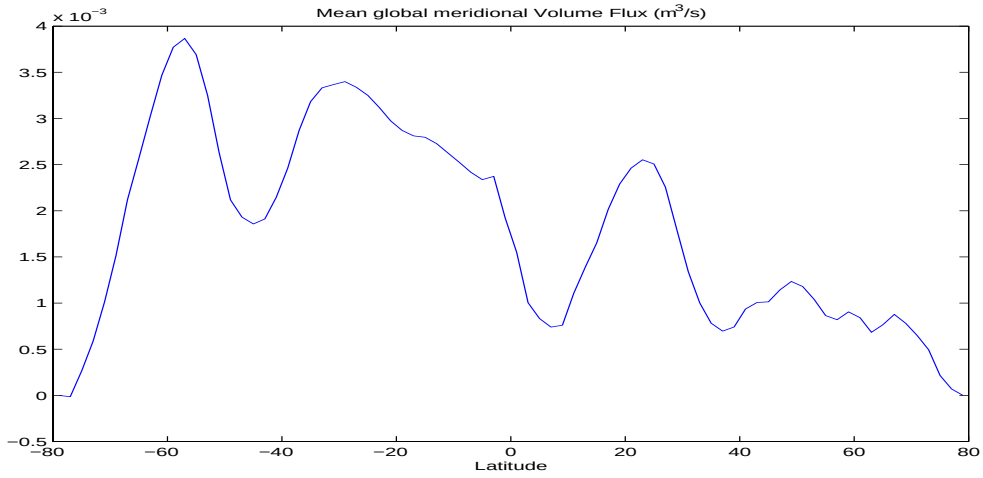
Mean global meridional Volume Flux (m3/s)
× 10−3
Latitude
4
3.5
3
2.5
2
1.5
1
0.5
0
−0.5
−80
−60
−40
−20
0
20
40
60
80

Figure 7:

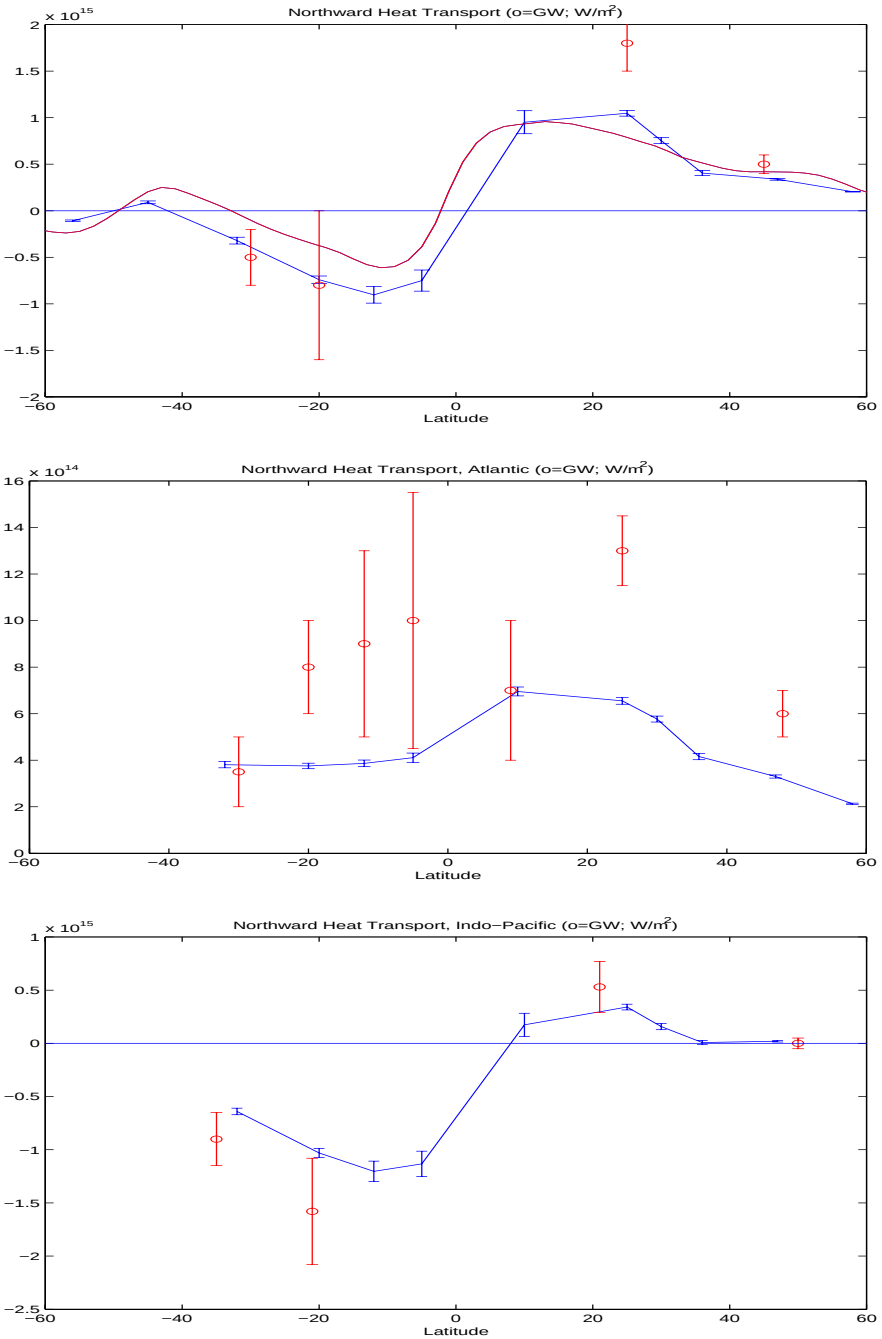
Northward Heat Transport (o=GW; W/m²)
x 10¹⁵
Latitude
Northward Heat Transport, Atlantic (o=GW; W/m²)
x 10¹⁴
Latitude
Northward Heat Transport, Indo−Pacific (o=GW; W/m²)
x 10¹⁵
Latitude

Figure 8:

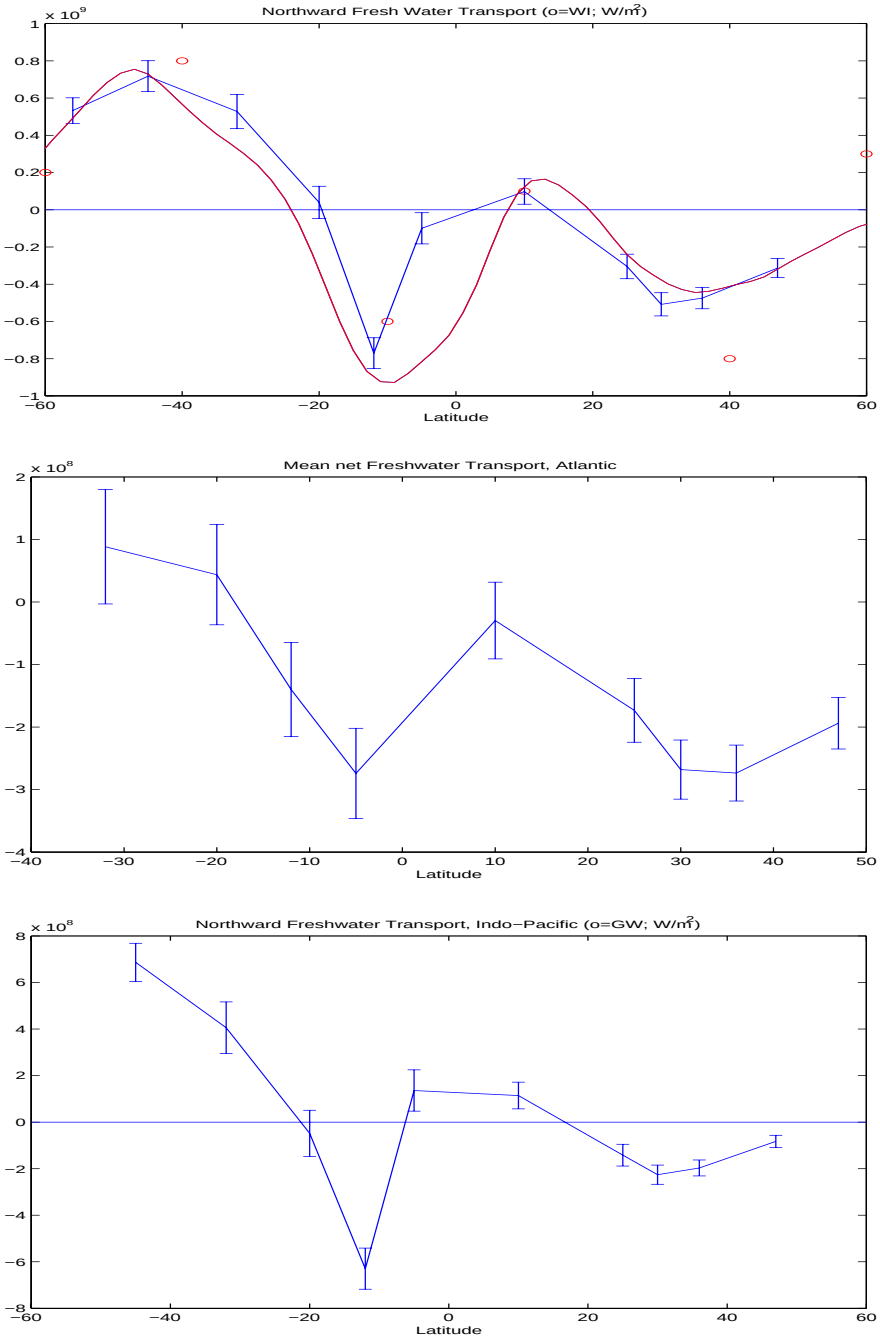
Northward Fresh Water Transport (o=WI; W/m2)
x 10^9
Latitude
Mean net Freshwater Transport, Atlantic
x 10^8
Latitude
Northward Freshwater Transport, Indo−Pacific (o=GW; W/m2)
x 10^8
Latitude

Figure 9:

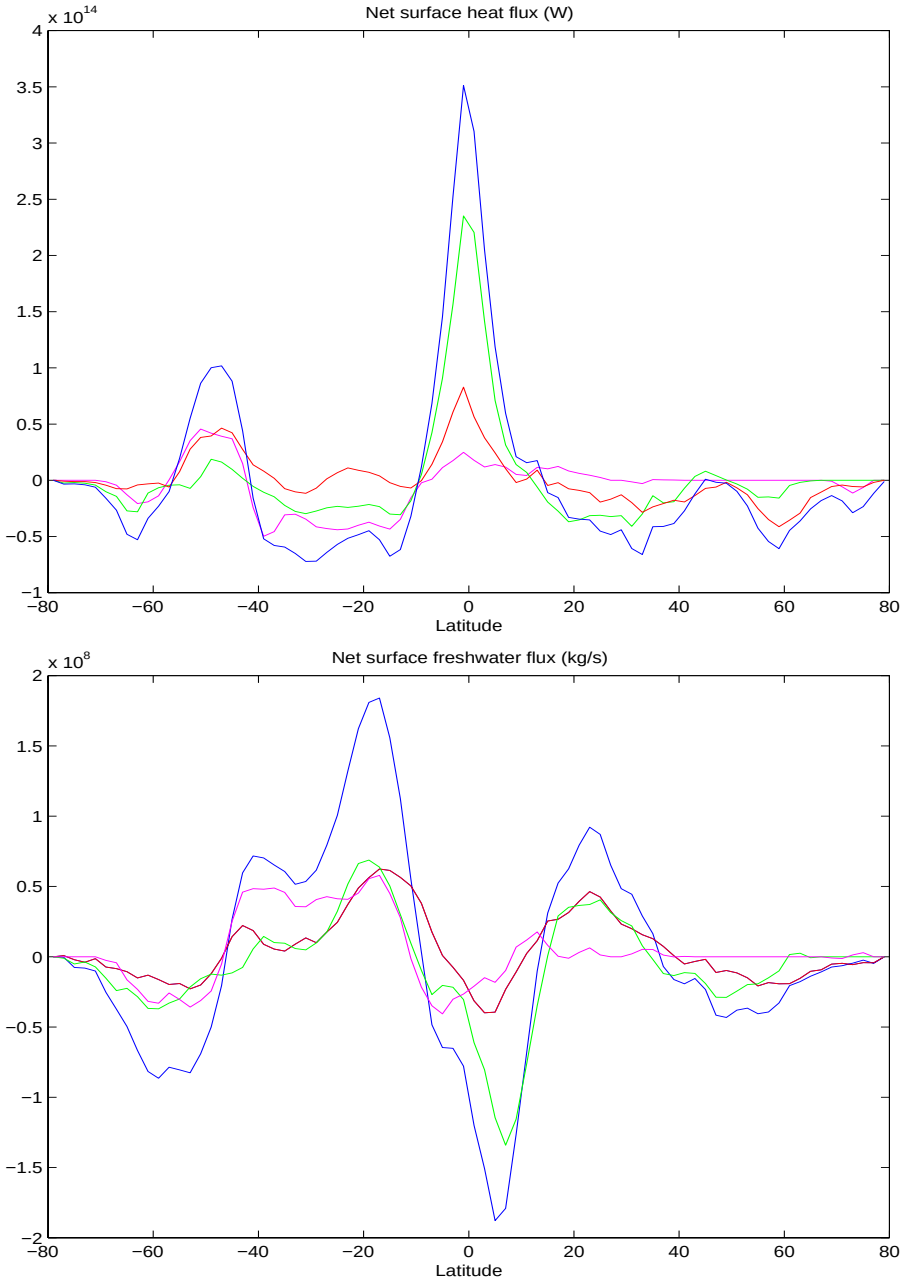
Net surface heat flux (W)
x 10^14
4
3.5
3
2.5
2
1.5
1
0.5
0
−0.5
−1
−80
−60
−40
−20
0
20
40
60
80
Latitude
Net surface freshwater flux (kg/s)
x 10^8
2
1.5
1
0.5
0
−0.5
−1
−1.5
−2
−80
−60
−40
−20
0
20
40
60
80
Latitude

Figure 10:

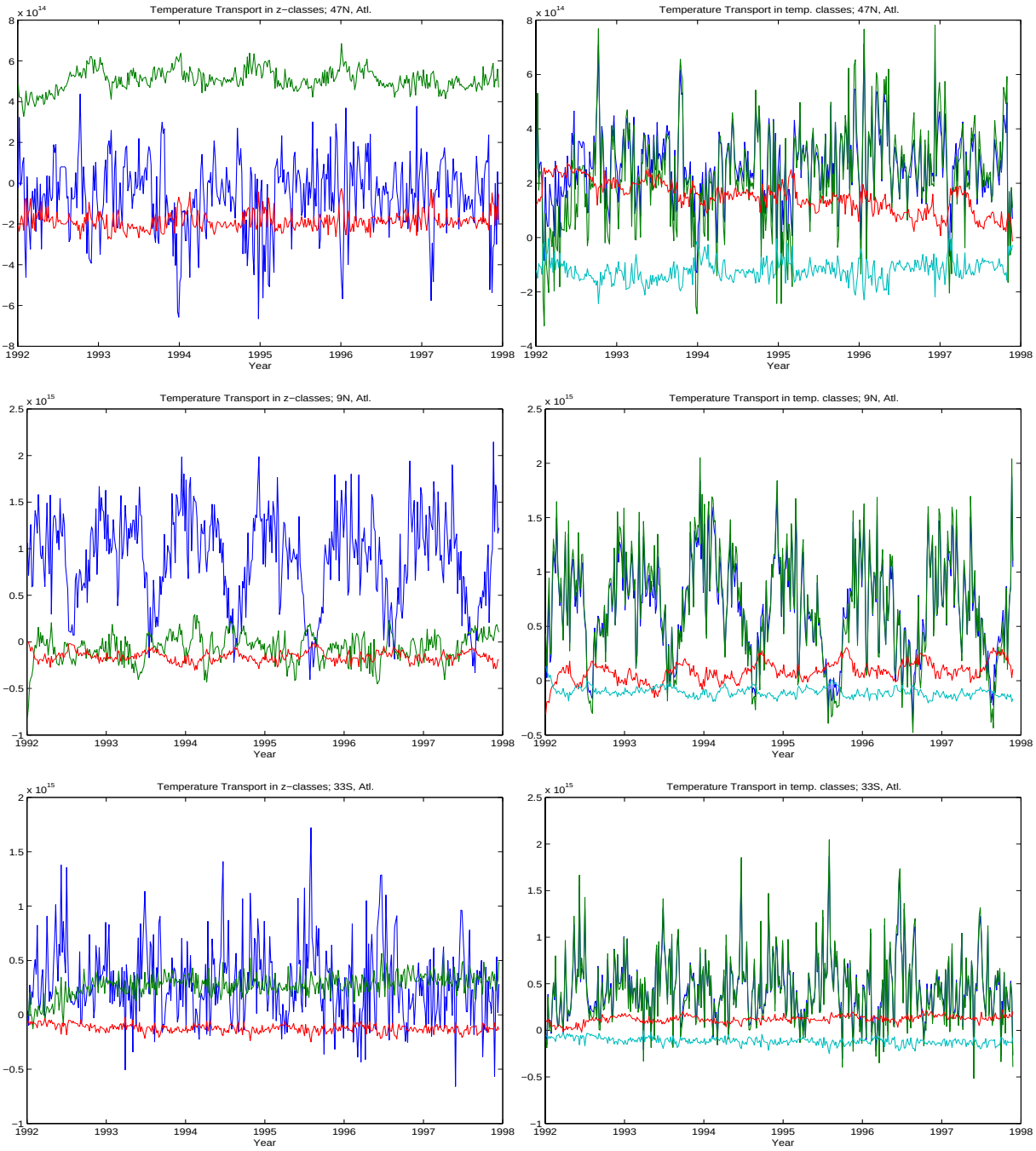
Temperature Transport in z−classes; 47N, Atl.
Temperature Transport in temp. classes; 47N, Atl.
Temperature Transport in z−classes; 9N, Atl.
Temperature Transport in temp. classes; 9N, Atl.
Temperature Transport in z−classes; 33S, Atl.
Temperature Transport in temp. classes; 33S, Atl.
Year

Figure 11:

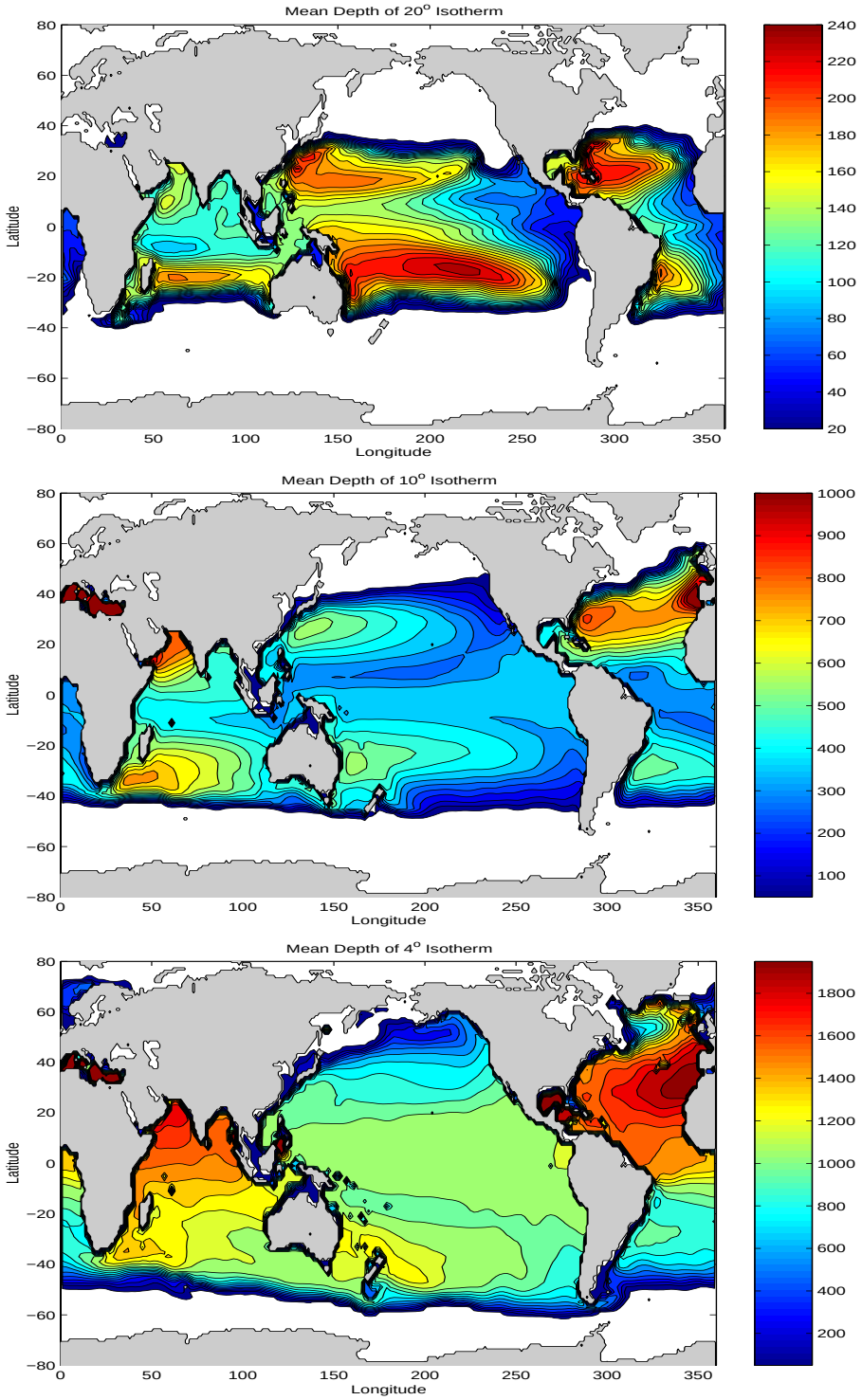
Mean Depth of 20° Isotherm
Latitude
Longitude
Mean Depth of 10° Isotherm
Latitude
Longitude
Mean Depth of 4° Isotherm
Latitude
Longitude

Figure 12:

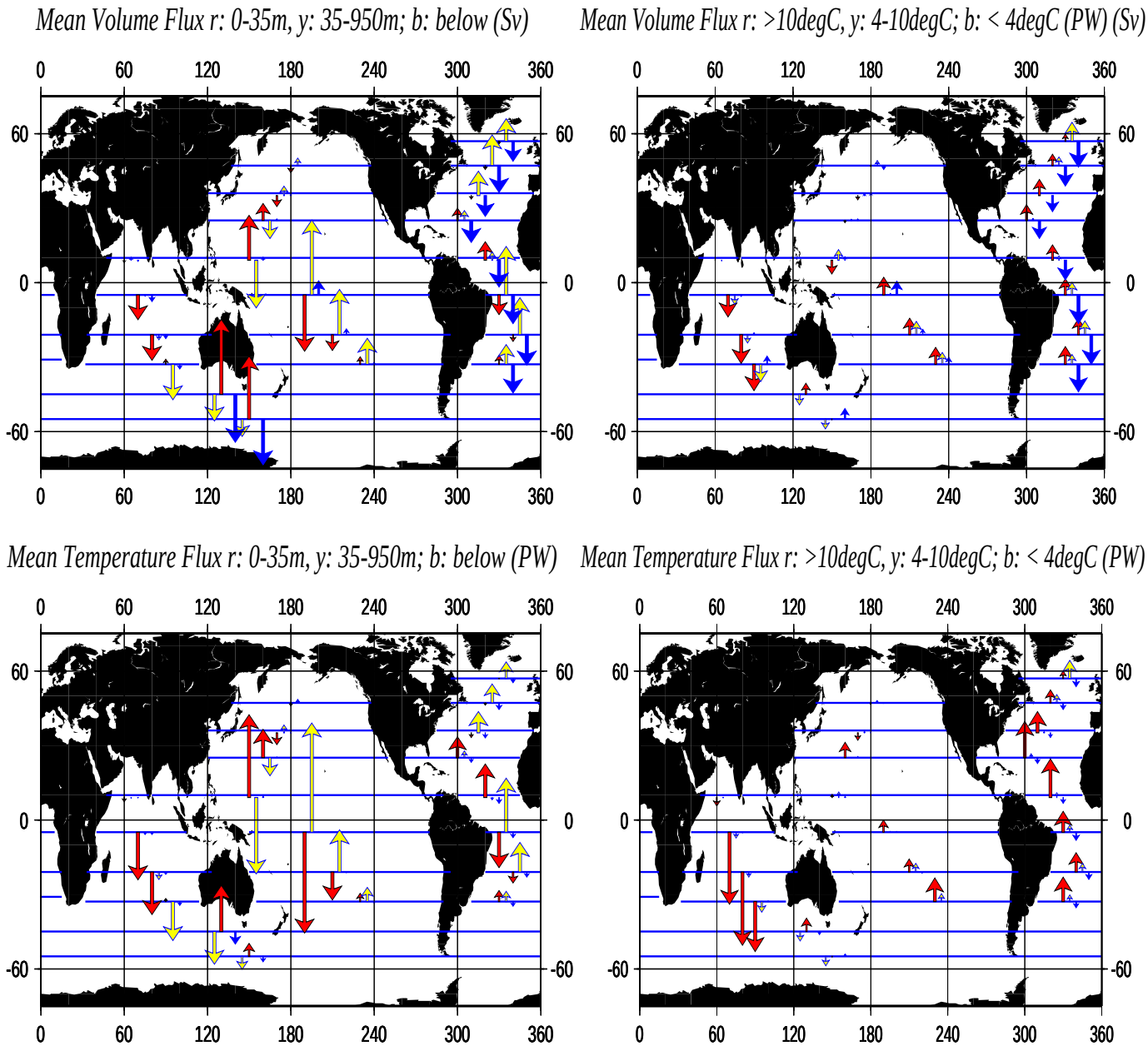
Mean Volume Flux r: 0-35m, y: 35-950m; b: below (Sv)
Mean Volume Flux r: >10degC, y: 4-10degC; b: < 4degC (PW) (Sv)
Mean Temperature Flux r: 0-35m, y: 35-950m; b: below (PW)
Mean Temperature Flux r: >10degC, y: 4-10degC; b: < 4degC (PW)
0 60 120 180 240 300 360
60
0
-60

Figure 13:

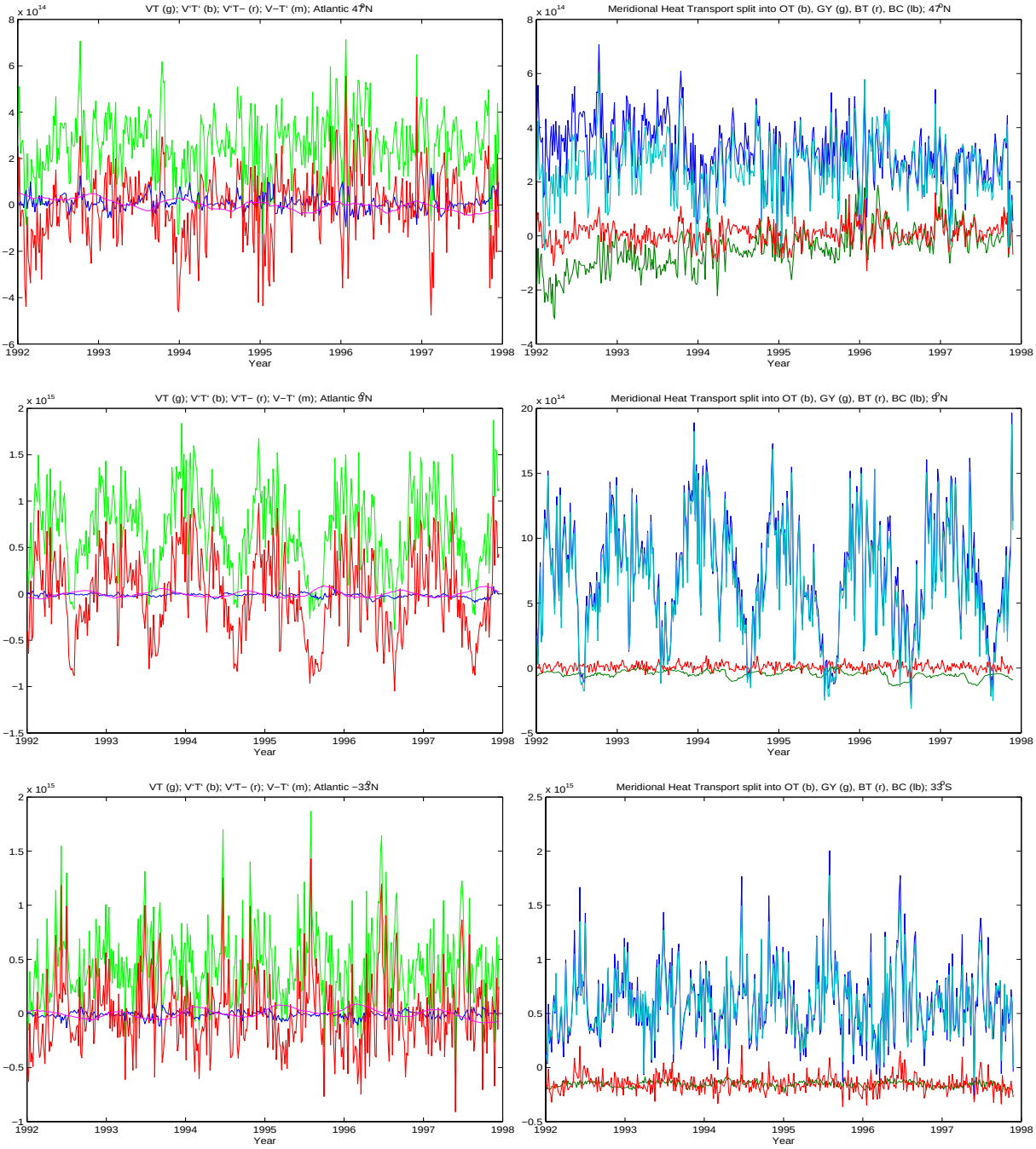
VT (g); V'T' (b); V'T− (r); V−T' (m); Atlantic 47°N
Meridional Heat Transport split into OT (b), GY (g), BT (r), BC (lb); 47°N
VT (g); V'T' (b); V'T− (r); V−T' (m); Atlantic 9°N
Meridional Heat Transport split into OT (b), GY (g), BT (r), BC (lb); 9°N
VT (g); V'T' (b); V'T− (r); V−T' (m); Atlantic −33°N
Meridional Heat Transport split into OT (b), GY (g), BT (r), BC (lb); 33°S
Year

Figure 14:

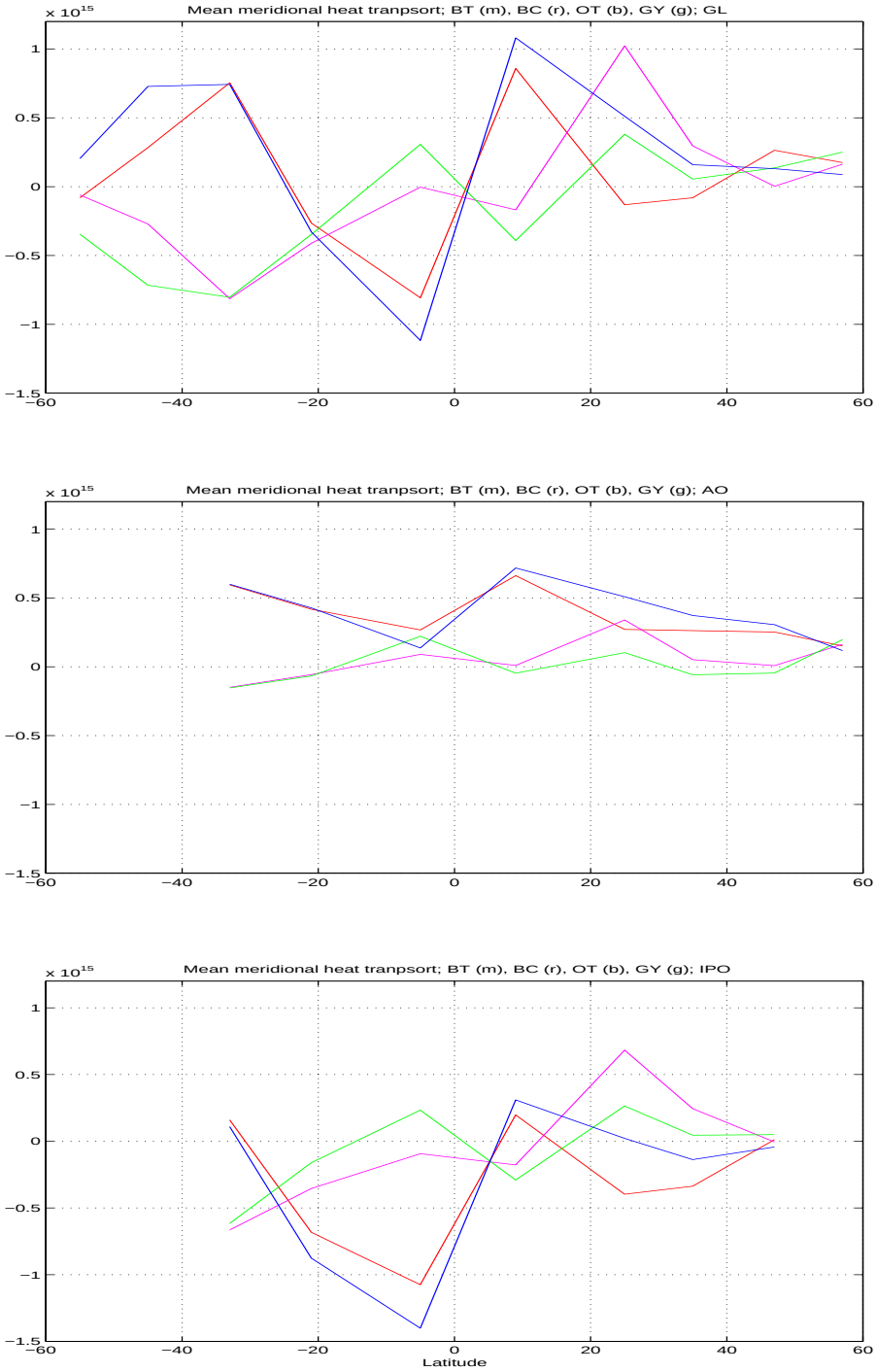
Mean meridional heat tranpsort; BT (m), BC (r), OT (b), GY (g); GL
× 10¹⁵
Mean meridional heat tranpsort; BT (m), BC (r), OT (b), GY (g); AO
× 10¹⁵
Mean meridional heat tranpsort; BT (m), BC (r), OT (b), GY (g); IPO
× 10¹⁵
Latitude

Figure 15:

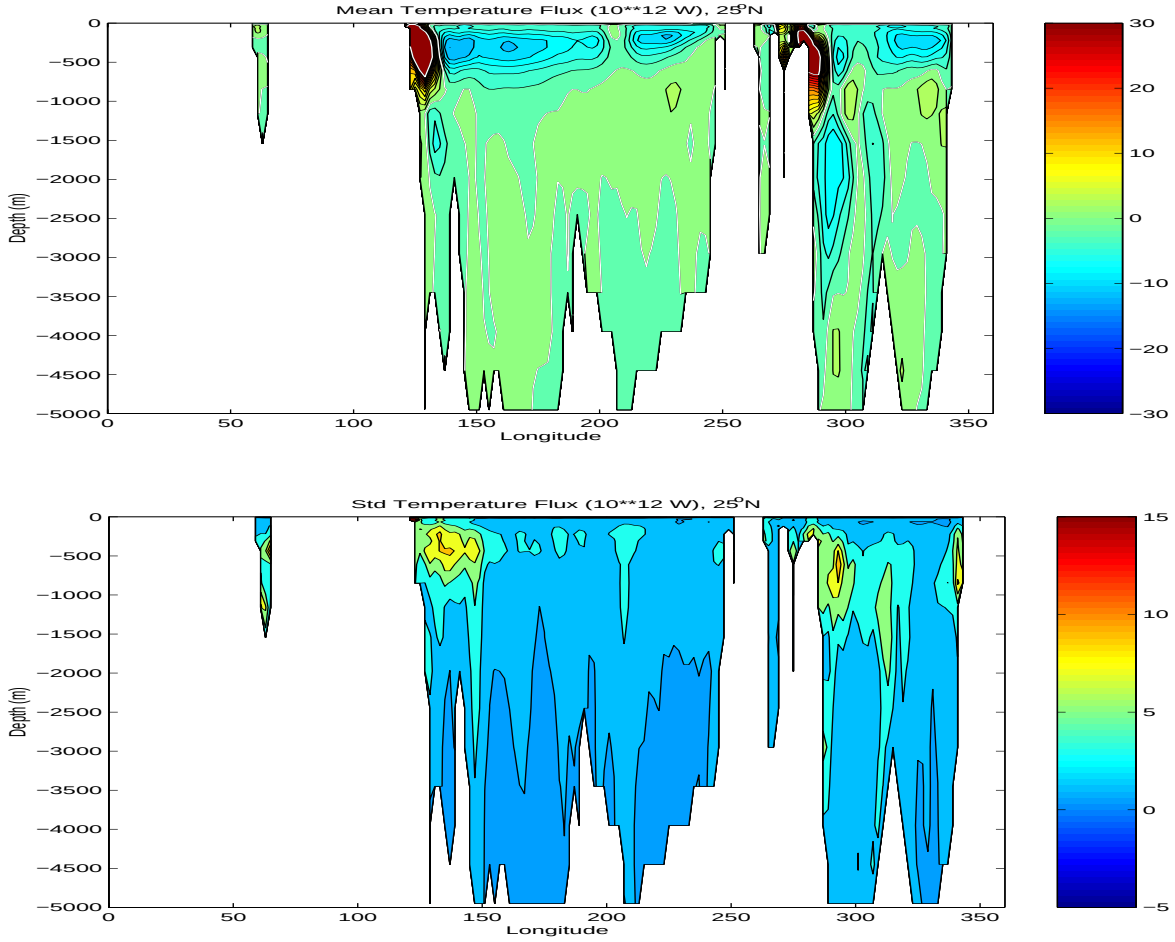
Mean Temperature Flux (10**12 W), 25°N
Depth (m)
Longitude
Std Temperature Flux (10**12 W), 25°N
Depth (m)
Longitude

Figure 16:

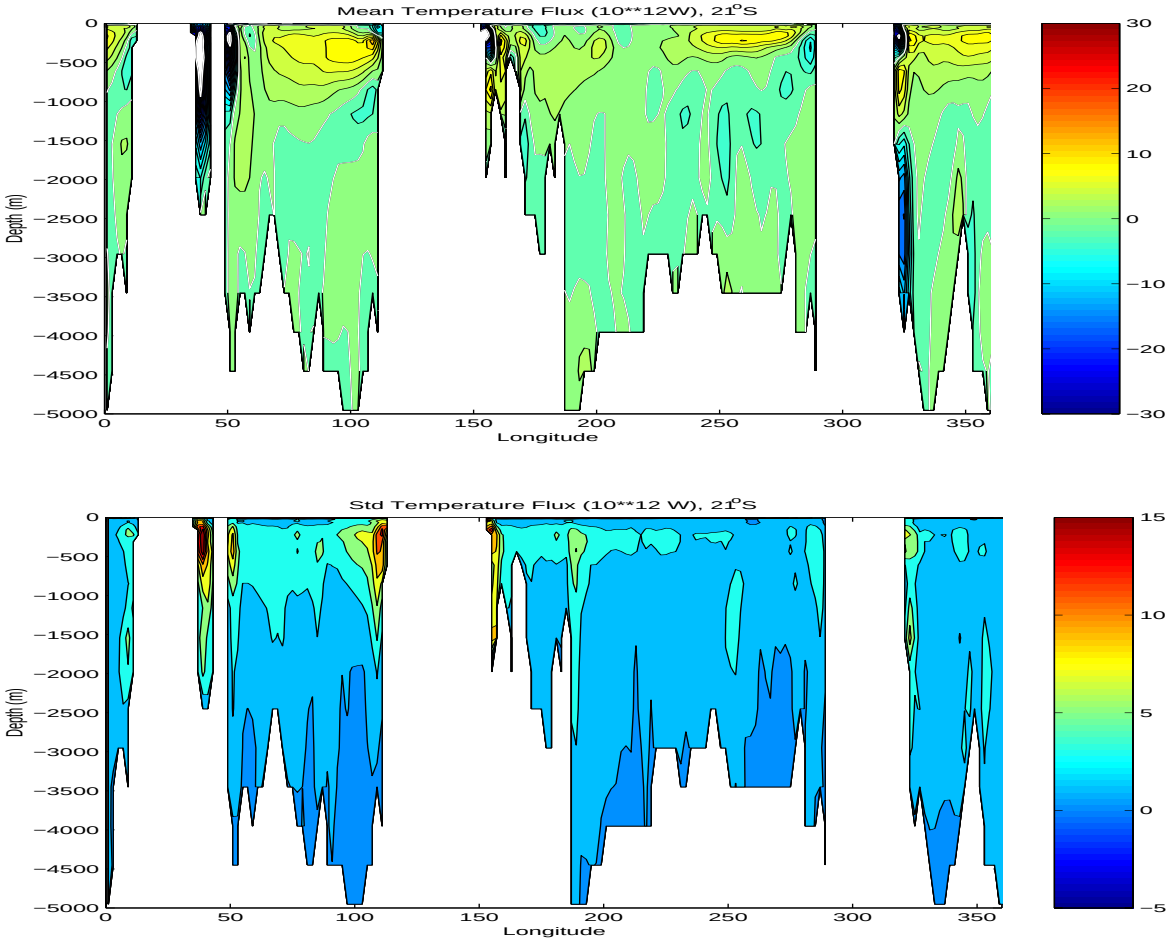
Mean Temperature Flux (10**12W), 21°S
Depth (m)
Longitude
Std Temperature Flux (10**12 W), 21°S
Depth (m)
Longitude

Figure 17:

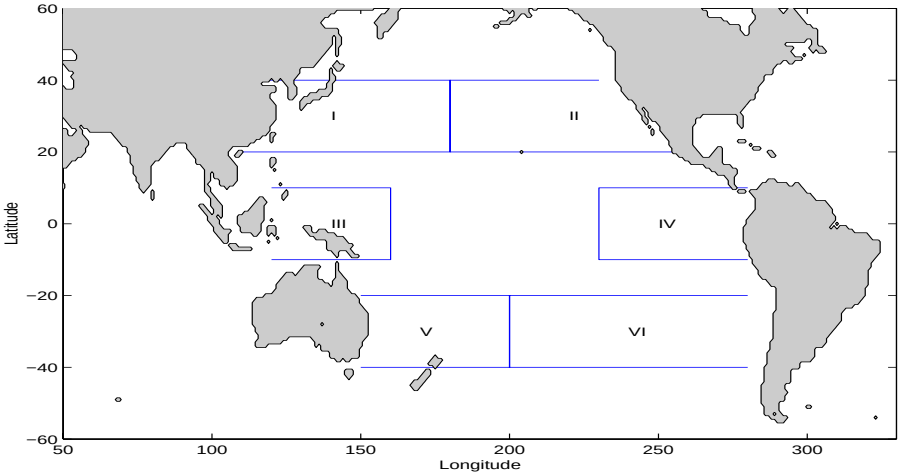
60
40
20
0
−20
−40
−60
50
100
150
200
250
300
Latitude
Longitude
I
II
III
IV
V
VI

Figure 18:

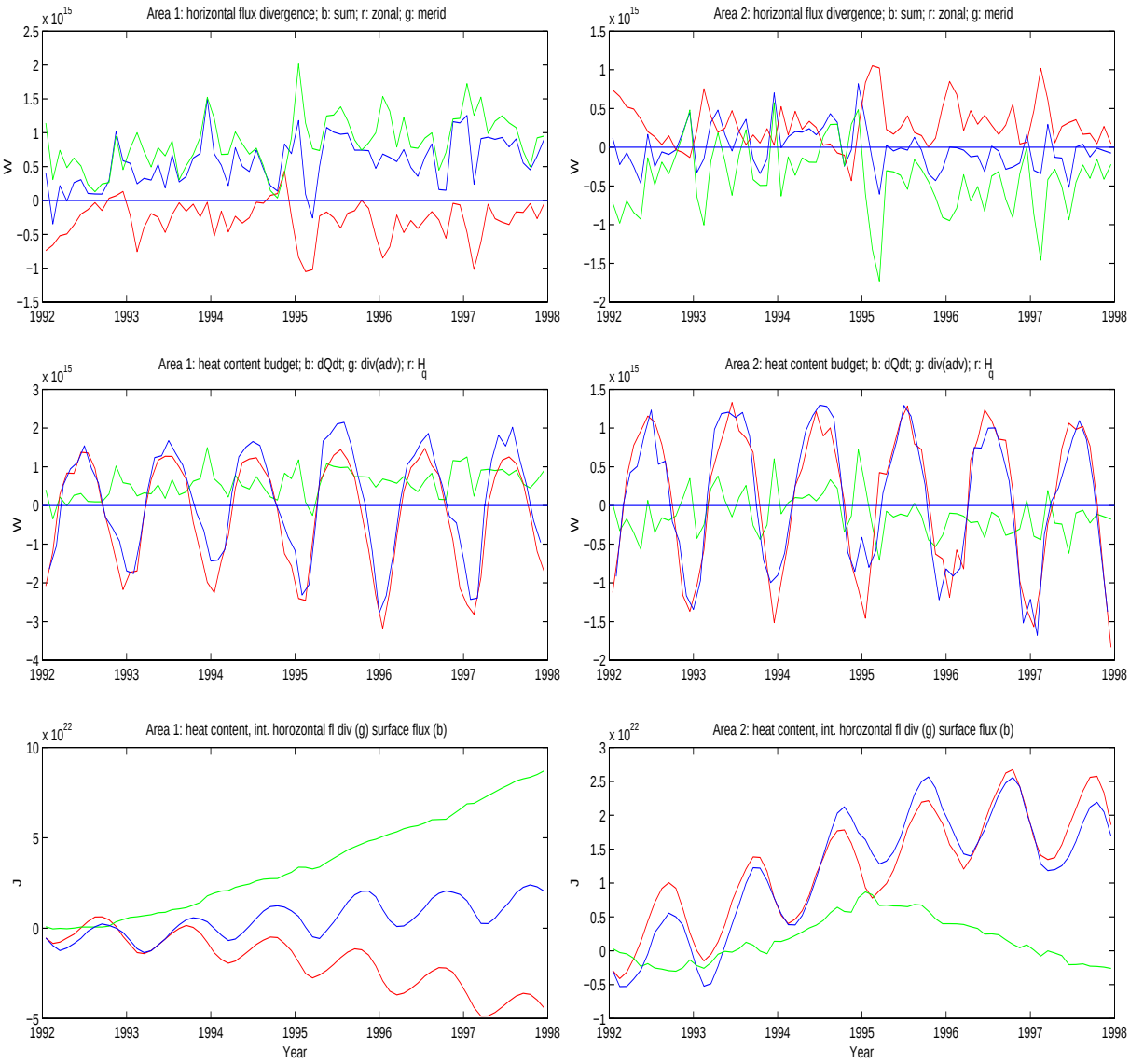
Area 1: horizontal flux divergence; b: sum; r: zonal; g: merid
Area 2: horizontal flux divergence; b: sum; r: zonal; g: merid
Area 1: heat content budget; b: dQdt; g: div(adv); r: Hq
Area 2: heat content budget; b: dQdt; g: div(adv); r: Hq
Area 1: heat content, int. horozontal fl div (g) surface flux (b)
Area 2: heat content, int. horozontal fl div (g) surface flux (b)
Year
Year

Figure 19:

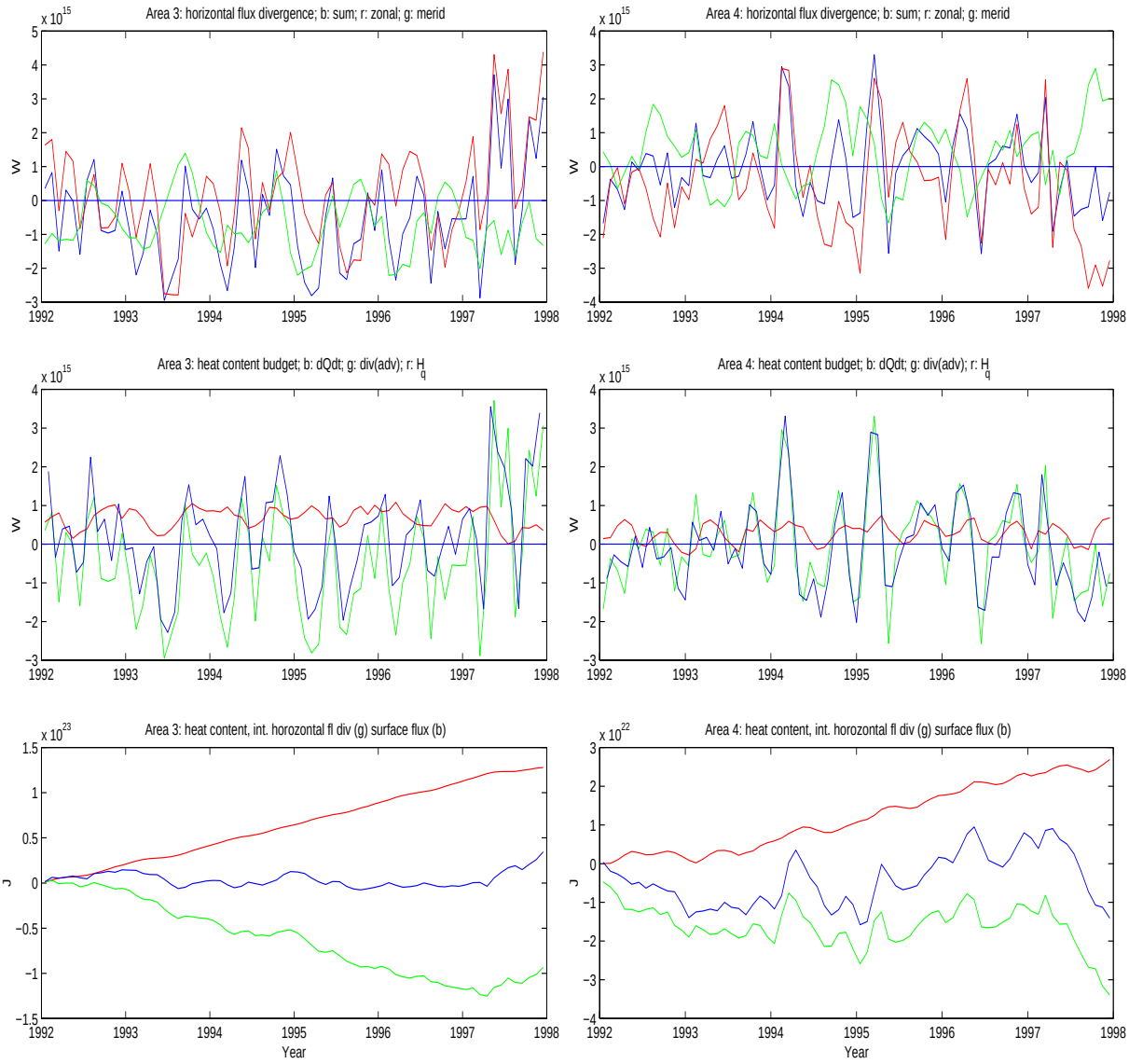
Area 3: horizontal flux divergence; b: sum; r: zonal; g: merid
Area 4: horizontal flux divergence; b: sum; r: zonal; g: merid
Area 3: heat content budget; b: dQdt; g: div(adv); r: Hq
Area 4: heat content budget; b: dQdt; g: div(adv); r: Hq
Area 3: heat content, int. horozontal fl div (g) surface flux (b)
Area 4: heat content, int. horozontal fl div (g) surface flux (b)
Year
Year

Figure 20:

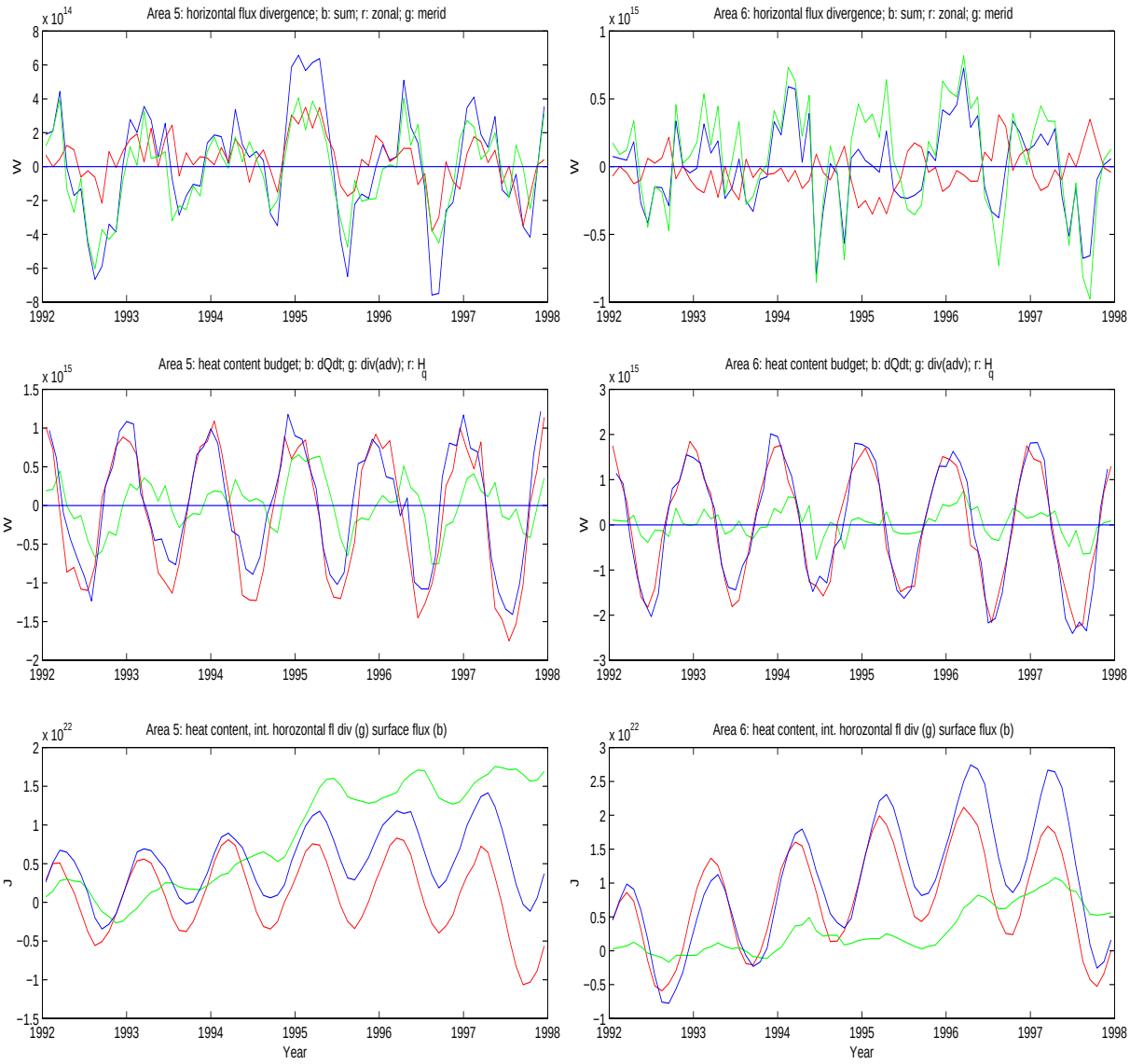
Area 5: horizontal flux divergence; b: sum; r: zonal; g: merid
x 10^14
Area 6: horizontal flux divergence; b: sum; r: zonal; g: merid
x 10^15
Area 5: heat content budget; b: dQdt; g: div(adv); r: Hq
x 10^15
Area 6: heat content budget; b: dQdt; g: div(adv); r: Hq
x 10^15
Area 5: heat content, int. horozontal fl div (g) surface flux (b)
x 10^22
Area 6: heat content, int. horozontal fl div (g) surface flux (b)
x 10^22
VV
J
Year
1992
1993
1994
1995
1996
1997
1998

Figure 21: